Effect of Variable Echo Spacing in Multi-Echo Sequences for Resolving Long T_2 Components in Multiple Sclerosis

Matthew Garrett Skinner

B.Sc. (Medical and Health Physics) McMaster University, 1999

A THESIS SUBMITTED IN PARTIAL FULFILLMENT OF

THE REQUIREMENTS FOR THE DEGREE OF

MASTER OF SCIENCE

in

THE FACULTY OF GRADUATE STUDIES

DEPARTMENT OF PHYSICS AND ASTRONOMY

We accept this thesis as conforming

to the required standard

THE UNIVERSITY OF BRITISH COLUMBIA

June 2001

In presenting this thesis in partial fulfilment of the requirements for an advanced degree at the University of British Columbia, I agree that the Library shall make it freely available for reference and study. I further agree that permission for extensive copying of this thesis for scholarly purposes may be granted by the head of my department or by his or her representatives. It is understood that copying or publication of this thesis for financial gain shall not be allowed without my written permission.

Department of Physics and Astronomy

The University of British Columbia
Vancouver, Canada

Date July 5/01

DE-6 (2/88)

Abstract

Five 48-echo CPMG pulse sequences were examined to determine their effectiveness in measuring the T_2 relaxation characteristics of cerebral tissue containing multiple sclerosis (MS) lesions. To this end, two sets of experiments were conducted in which the first 32 echoes had an echo spacing of 10 ms while the secondary echo spacing (SES), the final 16 echoes, was increased from 10 to 50 ms. In the first study 10 normal volunteers were imaged and the geometric mean T_2 (GM T_2), the peak widths and the myelin water fractions of the resultant T_2 distributions were measured and compared to the results of a previous study. The second study simulated the T_2 relaxation distributions that are expected in the brains of MS patients using a series of $NiCl_2$ water phantoms. The GM T_2, peak widths and myelin water fractions were measured in these phantoms.

The volunteer study showed that the T_2 distributions in several gray matter structures contained a single main peak (70 – 95 ms) with a low, or zero, myelin water fraction. The resolution of both myelin (10 – 50 ms) and intra/extracellular (70 – 95 ms) water peaks decreased while the accuracy of the GM T_2 of the main peak improved as SES increased. Sampling of the decay curves at longer times improved the separation of the short and intermediate T_2 compartments.

In the phantom study it was demonstrated that there was a clear clinical benefit to the use of a longer SES. When imaging lesions for which the T_2 of the intra/extracellular and lesion (200 – 500 ms) water compartments were separated by at least a factor of 3, each compartment in the distribution was better resolved when SES was increased. When the lesion T_2 was 179 ms, the intermediate and long T_2 peaks could not be resolved. The fraction that each component contributed to the mixtures also determined the resolution of their peaks. As the fractional contributions of each component increased so too did its resolution. Increased resolution of one component often resulted in better estimation of the other components. This study demonstrated that for specific clinical situations, it is advantageous to use extended secondary echo spacings for imaging the lesions of MS patients, without the risk of losing valuable short T_2 information.

Table of Contents

List of Tables

List of Figures

Glossary

Abbreviation	Meaning
2DFT	Two-dimensional Fourier transform
^{13}C	Carbon-13 nucleus
CP	Carr-Purcell
CPMG	Carr-Purcell-Meiboom-Gill
CSE	Conventional spin echo
CSF	Cerebrospinal fluid
^{19}F	Flourine-19 nucleus
FID	Free induction decay
FT	Fourier transform
^{1}H	Hydrogen nucleus
^{4}He	Helium-4 nucleus
GM T_2	Geometric mean T_2 relaxation time
MWF	Myelin water fraction
MRI	Magnetic resonance imaging
MS	Multiple sclerosis
^{23}Na	Sodium-23 nucleus
$NiCl_2$	Nickel chloride
NMR	Nuclear magnetic resonance
NNLS	Non-negative least squares
^{17}O	Oxygen-17 nucleus

^{31}P	Phosphorus-31 nucleus
PES	Primary echo spacing
RF	Radiofrequency
ROI	Region of interest
SES	Secondary echo spacing
SNR	Signal-to-Noise ratio
T_1	Spin-lattice relaxation time
T_2	Spin-spin relaxation time
TE	time to echo
TR	repetition time

Acknowledgements

This thesis could not have been completed without the help and the wisdom that I acquired from a number of people. First and foremost, I would like to sincerely thank my supervisor, Alex MacKay, for his assistance, support and generosity. Alex has taught me how to identify problems and more importantly how to solve them in a rational and logical way. He is also a great friend and I am grateful for allowing me the opportunity to be a member of this outstanding group. I would like to thank San Xiang, my second reader, for finding the time in difficult circumstances to edit my thesis.

Ken Whittall deserves tremendous recognition for offering his knowledge, skills and patience. Ken always found the time to sit down and work through a variety of problems with me. He provided me with the tools necessary to analyze my data and understand my results and his comments often inspired me tackle a problem from a different direction. I cannot express how appreciative I am Ken.

I would like to thank the colleagues I have worked alongside, Elana, Keith, Phil, Matt, Craig, Corree, David, Burkhard, Carl, Evan, Rachel, and Irene, for sharing their knowledge and for making this experience a memorable one. To my editors, Alex MacKay, Ken Whittall and especially Rachel Moll, thank you for giving up your valuable time to assist me in revising and correcting my thesis

I am very grateful to the UBC MRI technologists who spent many nights helping me to acquire my data and offering suggestions to optimize data collection. They also had the patience to teach me how to use the MRI scanner.

Last, but certainly not least, I would like to those closest to me. I have had the opportunity to meet many new people in graduate school, many of which will remain close friends of mine for a long time. To all of my friends, both new and old, I would like to sincerely thank you for all the good times we've had so far and for those we will have in the future. Thank you for your love, support and especially your patience. And finally, thank you mom, dad, Andrew, Kim and Jack for supporting me over distance and especially over time. Bill has finished!!!

Chapter 1 – Introduction

1.1 The Human Brain

The human brain is a complex yet highly organized structure responsible for motor control, consciousness and behaviour. It occupies a volume of approximately 1 350 cm^3 and contains nearly 100 billion neurons [1]. Nearly 10 to 100 trillion points of cellular contact exist between these 100 billion neurons. The brain is principally composed of two broad classes of cells: *neurons* and *glia*. Neurons are the nervous system cells that process and exchange information and are responsible for behaviour. The principle role of glial cells is to provide mechanical and metabolic support for neurons, but are not known to function in information transfer.

Neurons are structurally diverse, and vary widely in both size and form. They may be as small as 0.1 mm in length, such as in the cortex of the central nervous system (CNS), or as long as 1 m, such as those that descend into the spinal cord. The neuron can be described by four functionally distinct subunits, as shown in figure 1.1. The cell body, or soma, contains the nucleus and is responsible for metabolic activity. The dendrite's primary role is to receive signals from other cells and transfer the incoming information to the soma for processing. The high degree of branching of the dendrites increases the receptive area of the neuron, allowing it to receive information from an immense number of surrounding neurons. A single CNS neuron may receive input from tens of thousands other of neurons [2]. The axon carries information away from the soma to other neurons or, in the peripheral nervous system (PNS), to neurons and muscle cells. Individual axons can propagate signals for up to 1 m and their diameters may vary from 0.2 to 20 μm. The final subunit is the axon terminal, which receives signals from the axon and releases specific neurotransmitters to other cells.

The point of communication between cells is called the synapse. Synapses are normally unidirectional so that activity at the axon terminal of the neuron that transmits the information (presynaptic cell) will affect the behaviour of

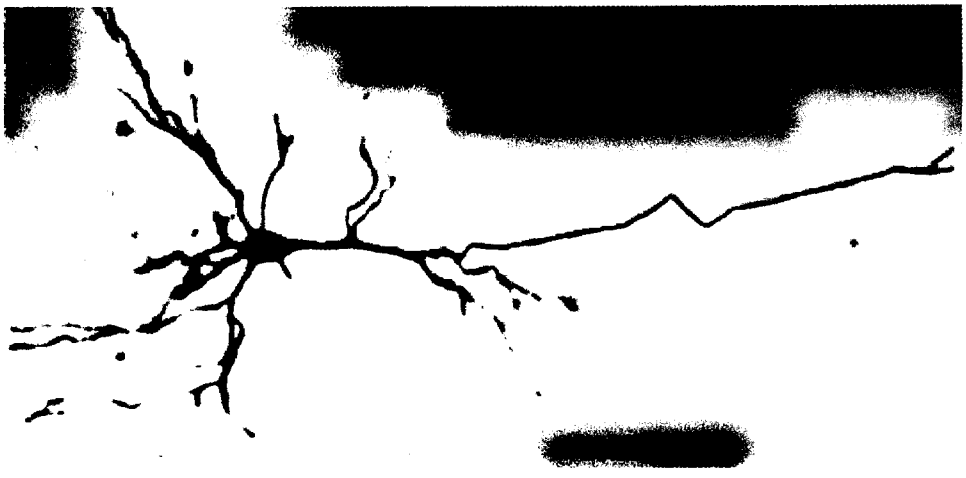

Figure 1.1: A typical central nervous system neuron. The soma is the circular structure to the left of center. Dendrites are the short extensions protruding radially from the soma. The axon extends horizontally from the soma across the image to the right. The axon terminal is at the distal end of the axon.

the receiving cell (postsynaptic cell). Postsynaptic membranes are normally located on the cell body or on the dendrites of the postsynaptic cell. However, synapses between axons are known to occur [1].

Whereas neurons receive and transmit information throughout the brain and to the body, the role of glial cells is principally mechanical and metabolic in nature. Although they outnumber neurons by nearly 50:1, their small size means that they account for only half of the brain's weight. Glial cells can be separated into three groups. The astrocytes, found only in the CNS, provide neurons with structural support and help control their chemical and ionic extracellular environment. Oligodendrocytes, of the CNS, and Schwann cells, of the PNS, offer electrical insulation to neurons through the production of myelin. In the CNS a single oligodendrocyte can myelinate up to 40 different axons [1, 3].

1.2 Myelin and Signal Propagation

The myelin sheath is a lipid-protein membrane, deposited by oligodendrocytes in the CNS or Schwann cells in the PNS, which surrounds axons in tightly wound layers. The electron micrograph in figure 1.2 clearly demonstrates how tightly bundled the multiple myelin layers are. In the CNS, the myelination of an axon occurs when the oligodendrocyte extends from its tip. The tip lies against the axon and as it elongates, it pushes underneath previous

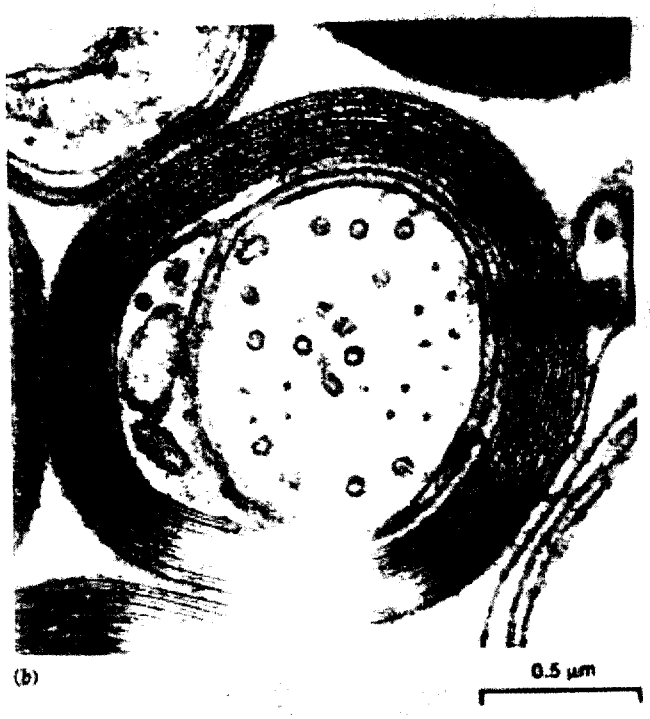

Figure 1.2: An electron micrograph of a myelinated axon. The axon is the large circular structure in the center of the image. The dark concentric rings surrounding it are the layers of myelin deposited by an oligodendrocyte.

layers. An axon is normally myelinated by multiple oligodendrocytes with each myelinated region being separated by small space absent of myelin. These spaces are known as the *nodes of Ranvier* and they contain the vast majority of voltage-gated Na^+ channels because here the nodes are in direct contact with the extracellular fluid. The channels are responsible for amplification and propagation of action potentials along the axon.

An action potential is a brief pulse of current that temporarily depolarizes the neuron's plasma membrane. The depolarization causes the voltage-gated Na^+ channels to open. The opening of voltage-gated channels permits Na^+ ions to enter the cell along an electrochemical gradient. The influx of positive charge results in further depolarization, allowing more Na^+ to enter. This self-amplifying depolarization affects neighbouring regions of the membrane, causing them to depolarize. The sequence of depolarization and the influx of Na^+ ions continues unidirectionally along the length of the axon. In a small, unmyelinated nerve fiber, signals are transmitted much a slower velocity via passive depolarization of

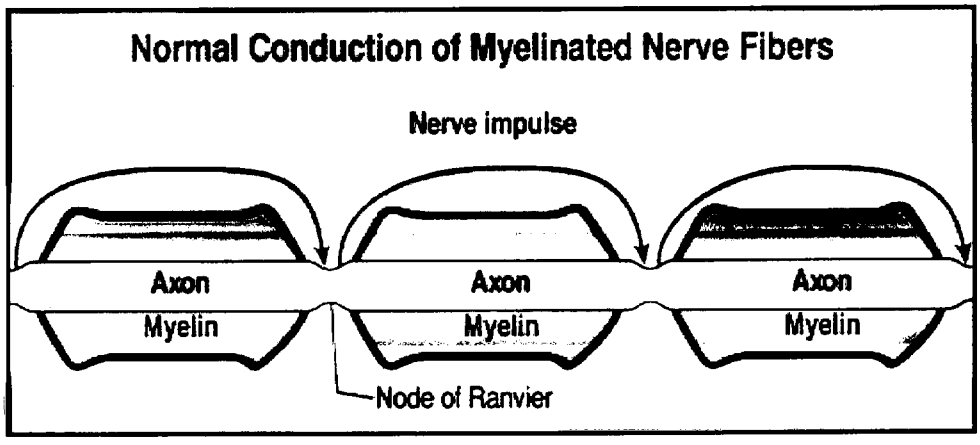

Figure 1.3: Saltatory conduction in normal myelinated neurons. The action potential jumps along the axon, from one node to the next. This method greatly speeds up the conduction of action potentials.

neighbouring regions. Due to the slow conduction velocity, the use of unmyelinated fibers is generally restricted to short distances.

For long-distance communication however, passive depolarization is far too slow and inefficient. Instead, active signalling is employed, which takes advantage of the insulative properties of myelin to transmit information without attenuation at velocities up 100 m/s [3]. These velocities are compared to velocities of 0.4 m/s found in small-diameter, unmyelinated fibers. The ensheathed portions of the axon are so well insulated that a depolarization of one node almost immediately spreads passively to the next node where another action potential is generated. The rapid depolarization is due to the myelinated sections, which permit virtually no current leaks across the membrane. The high density of voltage-gated Na^+ channels at each node results in a rapid depolarization of that node when the threshold stimulus is reached. At each node action potentials are created anew but can not be generated between nodes because the insulation prevents the threshold level of depolarization from being achieved. Therefore, the action potential travels along an axon from one region of depolarization to the next, jumping from node to node in a process known as *saltatory conduction.* Action potentials are shown travelling from node to node along a myelinated axon in figure 1.3.

Saltatory conduction is the principle means of communication throughout the nervous system because many signals are required to travel from the control

centers in the brain out to the extremities. When a disruption in the wiring of the brain occurs, motor control or neurological dysfunction is often a result. In the next section, one of the most common such neurological disorders, multiple sclerosis (MS), will be discussed.

1.3 Multiple Sclerosis

Multiple sclerosis (MS) is an unpredictable, at times disabling, disease of the central nervous system. It is a major cause of severe and chronic disability in young adults as it typically begins in early adulthood. An estimated 50,000 Canadians and 300 000 Americans currently are afflicted with MS [4]. Prevalence rates range from one MS case per 500 people to one in 1,000 across the country. As MS tends to occur more often further away from the equator, countries such as Canada are regions of high risk for MS.

Two primary forms of the disease exist. The acute form afflicts 10 % of patients and is characterized by rapid and progressive demyelination of CNS axons. The chronic form is recognized as a relapsing-remitting cycle where patients experience short periods of symptoms. Between the onset of symptoms patients do not experience an increase in clinical disability. The chronic form affects 90 % of MS patients.

MS is generally believed to be a cell-mediated, auto-immune disorder that occurs in genetically susceptible people [5]. Genetic factors are believed to be involved in MS susceptibility based on studies involving monozygotic and dizygotic twins [6, 7]. These showed increased risks in monozygotic twins and also demonstrated a twenty-fold increase in developing MS in the relatives of patients, compared with the general population. Unfortunately, the early sequence of events causing the onset of disease is largely unknown and the subject of current research.

Pathologically, the signature of MS is the demyelinated plaque. These plagues are well-demarcated hypocellular regions and are principally located within the white matter of the brain. These regions are distinguished primarily by a loss of myelin and accompanied by astrocytic scars and a relative preservation

of axons. Pathological studies indicate the initial event in the formation of MS lesions is a disruption in the blood-brain barrier (BBB), which triggers an inflammatory response by lymphocytes and monocytes [8, 9]. They are recruited across the BBB and attack the myelin sheath surrounding the axons. In new, active lesions, the primary characteristic is inflammation with various stages of demyelination [10]. Chronic lesions display ongoing inflammation and advancing demyelination. Chronic lesions represent a more permanent and irreversible stage of tissue damage than do active lesions [11]. Recent studies have shown that in addition to demyelination, early stages of MS indicate axonal loss is a contributor to clinical deficit [12 - 14].

Diseases such as MS demonstrate the neurological effect of demyelination of the axons. Symptoms of MS, such as fatigue, balance and coordination problems, muscle stiffness and weakness, are consequences of decreased motor control because of the disruption signaling pathways. In figure 1.4 the disruption in the propagation of an action potential is illustrated. It is thus desirable to have a clinical tool that allows a physician to monitor the degradation of the white matter because this will assist in early diagnosis of diseases like MS. The development of magnetic resonance imaging (MRI) has permitted *in-vivo* diagnosis of MS and has allowed patients to be identified earlier in the clinical course of the disease.

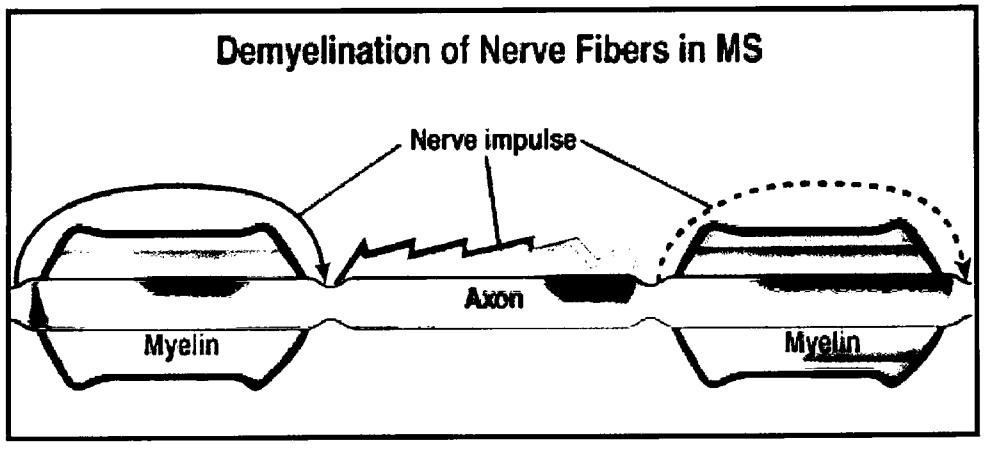

Figure 1.4: Saltatory conduction in a demyelinated neuron. The action potential encounters a demyelinated region of the axon and is slowed down as it must passively move along the axon to the next node. This results in decreased motor control as fewer action potentials are conducted.

1.4 Previous Studies in MS using Magnetic Resonance Imaging (MRI)

Conventional MRI has become established as the most important paraclinical tool for diagnosing MS, visualizing the dynamics of lesion formation and monitoring the efficacy of experimental treatments. Because demyelination is a hallmark of lesion formation and growth, efforts are being made to develop MRI pulse sequences that permit measurement of the amount of myelin present within the brain. These techniques take advantage of known alterations in the T_2 relaxation characteristics in regions where lesion formation is occurring.

Previously, Dr. MacKay's MS/MRI research group at the University of British Columbia demonstrated that water in the brain is separable into three principle components [15, 16]. A key aspect of the work was the ability to isolate a fast relaxing component of the T_2 decay curve that was previously unresolved from the main cytoplasmic water component. The three principle water environments have now been indentified as: 1) a short T_2 component, between 10 and 50 ms, due to water compartmentalized in myelin bilayers; 2)an intermediate component, between 70 and 95 ms, arising from cytoplasmic water; 3) a component with at a T_2 greater than 1 s, caused by water of high mobility within cerebrospinal fluid (CSF). The short component has also been observed in other *in-vitro* [17 - 21] and *in-vivo* [22, 23] studies of CNS tissue. It is believed that the amount of water between the myelin bilayers is directly proportional to the amount of myelin present. A T_2 distribution showing these three distinct regions is illustrated in figure 1.5.

Identification of a specific myelin component to the T_2 distribution has allowed quantification of myelin in the normal population and patients with MS. This is accomplished through calculating the myelin water fraction (MWF). The MWF is defined as the ratio of the signal from the short T_2 component to the signal from the entire T_2 distribution. Visualization of demyelinated regions can be accomplished through generation of myelin maps, figure 1.6, which can be used clinically to identify the location and boundaries of lesions. The areas of

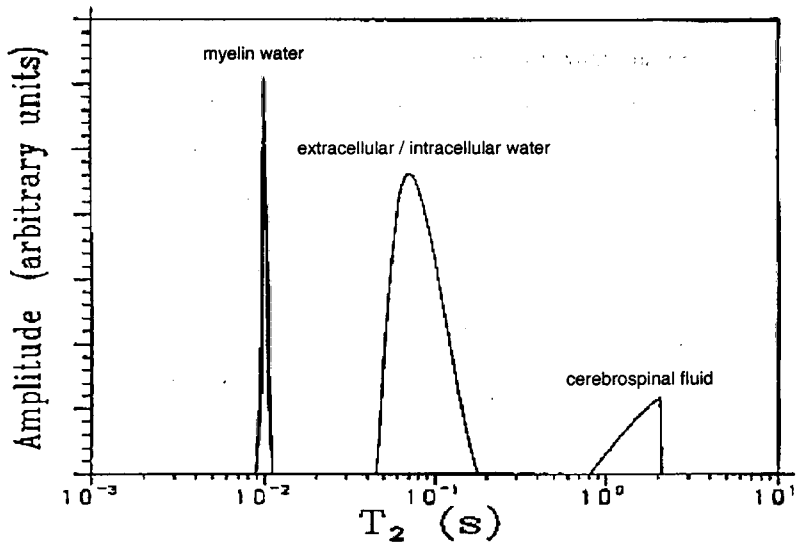

Figure 1.5: A T_2 distribution showing the three principal water compartments in a normal subject. The compartmentalized myelin water has a narrow peak positioned between 10 and 50 ms. CSF has a long T_2 relaxation as shown at 1s.

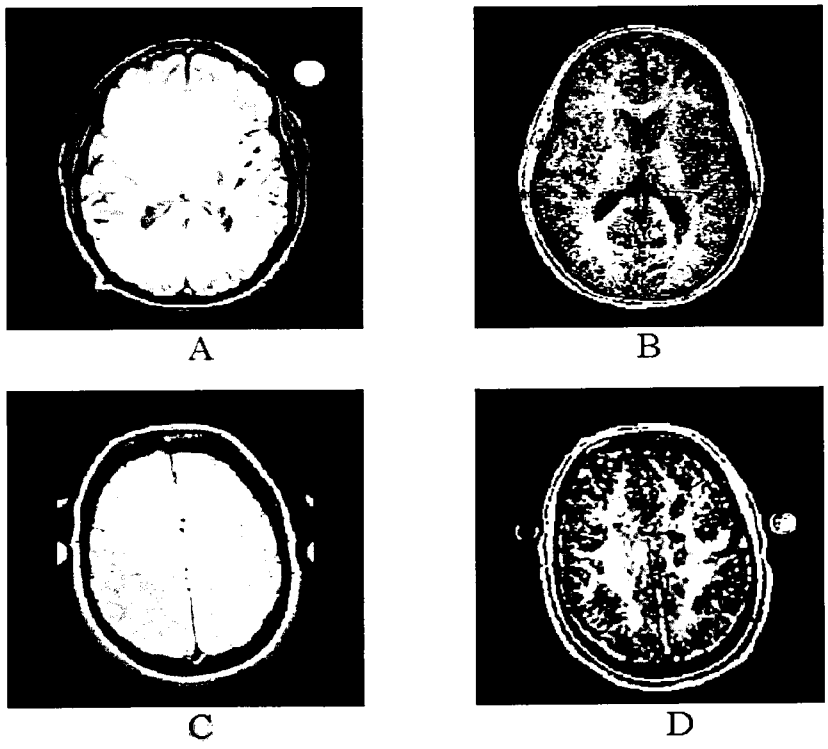

Figure 1.6: Conventional spin echo images (a, c) and corresponding myelin maps (b, d) of a normal subject and an MS patient. In the normal subject, white matter is dark in a) and the corresponding regions of myelin are brightest on the myelin map in b). In MS lesions, demyelinated regions of the white matter appear bright in c) and dark on the myelin map d)

increased signal on the myelin map represent regions of the brain with increased myelin and correlate very well to the white matter.

A 1997 study, led by Dr. Whittall, measured the mean water content, MWF and the T_2 distributions six gray and five white matter structures using a non-negative least squares method of relaxation analysis [16, 24]. They demonstrated that there was sizeable difference in all three values in different brain structures. They also showed that the greatest MWFs were found predominantly within the white matter [16].

Other studies have shown that the brains of MS patients have additional T_2 components in their T_2 distributions. These components occur at relaxation times that are between 3 and 5 times longer than cytoplasmic water compartment [25 – 28]. These studies measured the decay curves to be biexponential in nature and could not detect the short T_2 component arising from compartmentalized myelin water. It has been shown that normal appearing white matter (NAWM) in MS patients also has an increase in both T_1 and T_2 relaxation times [25]. Although these studies varied in the pulse sequences employed and the method of relaxation analysis the conclusion that there exists a long T_2 component in MS patients remains.

1.5 Motivation

While previous studies have demonstrated the existence of a short T_2 component due to myelin water, others have shown a long T_2 component due to MS lesions. Few studies have had the ability to accurately resolve both peaks in the T_2 distribution because of conflicts within the pulse sequences. Ideally, a pulse sequence needs to be able to sample many points in a short period of time at the beginning in order to accurately measure the fast relaxing component. However, it also needs to sample many points later in time when the long T_2 component is relaxing.

Dr. MacKay has modified a 32-echo pulse sequence to allow collection of 48 echoes for greater sampling. A feature of the 48-echo sequence is that it is possible to split the echo train into two sections, each with its own echo spacing. The goal of our research was to optimize this 48-echo sequence in terms of the

second echo spacing to allow complete sampling of the T_2 decay curves. We chose to manipulate the echo spacings such that at early times following the excitation pulse, the decay curve was sampled with 10 ms echo spacing for the first 32 echoes. The 10 ms echo spacing facilitates collecting maximum information about the myelin and intra/extracellular water components. We then chose and tested different echo spacings for the final 16 echoes. These ranged from 10 ms up 50 ms. As previous studies have indicated that MS lesions have a long T_2 relaxation time on the order of 500 ms, sampling the decay curve later in time should result in greater accuracy in identifying T_2 of MS lesions. By optimizing these final 16 echoes, it was our hypothesis that we could discover a pulse sequence that would show the myelin, intra/extracellular and lesion water compartments in MS patients.

1.6 Overview of Thesis

Two complementary studies were undertaken in this thesis to evaluate the effect of altering a 48-echo CPMG pulse sequence that would allow multiple echo spacings to be used for imaging. The goal of the study was to determine the optimal pulse sequence for imaging the brains of patients with MS. To achieve this goal, two sets of experiments were performed. First, normal volunteers were imaged to ensure the various sequences tested did not result in anomalous, unexpected results. To mimic the behaviour of MS lesions, a set of water based phantoms were studied to find the optimal sequence that could be used in a clinical setting.

The necessary concepts of nuclear magnetic resonance and image acquisition in magnetic resonance imaging are introduced in chapter 2. The materials and methods that were used are provided in chapter 3. These will include a description of the brain structures of interest from the *in-vivo* study and the composition of the phantoms that were used to mimic MS lesions. An outline of the algorithm, non-negative least squares, used to generate the T_2 distributions based on the measured signal will also be presented. The results from the *in-vivo* study on the normal volunteers are presented in chapter 4, while

the phantom results are shown in chapter 5. Finally, in chapter 6 the main conclusions are given and suggestions are provided for the optimal pulse sequences to be used in different clinical situations where MS lesions are to be studied. A brief discussion of the future work that stems from our research is also addressed.

Chapter 2 - NMR Theory and Basics of MRI

2.1 Historical Overview of Magnetism

Magnetism was discovered and described nearly 3000 years ago as a mysterious attraction or repulsion that was felt between different stones. As far back as 800 B.C., Greek literature describes the mineral magnetite (Fe_3O_4) and its magnetic properties, such as its ability to attract pieces of iron. The English first developed lodestone for use in compasses as early as the 13th century, however the cause of the forces that made the compass needle point to North were not yet understood. In 1269, Pierre de Maricourt mapped out the directions taken by a needle when placed at various points on the surface of the sphere. He found that the directions formed lines that encircle the sphere passing through two points that were diametrically opposite to each other and called these poles. He showed that for all magnets, regardless of size or shape, there existed two poles, and they exerted forces that were similar to those from electrical charges [29]. Ørsted published results in 1820 that demonstrated a relationship between electricity and magnetism. When an electric current was passed through a wire it caused a nearby compass needle to be deflected [30]. Later studies by Weber, Arago and Amp re indicated that conductors through which current were passed, could cause each other to move without being in physical contact. A field had been established around electric currents that interacted with the field created by the second conductor. Amp re developed quantitative laws of magnetic force between current-carrying conductors and suggested that molecular sized electric current loops were the cause of all magnetic phenomena, the basis for the modern theory of magnetism. Through these experiments it was concluded that magnetism was similar in effect to other phenomena such as electrostatics and gravity that exhibited 'action at a distance'.

The relationship between magnetic and electrostatic forces was established early in the 20th century through Einstein's special theory of relativity. Meanwhile, the development of quantum mechanics led to the

discovery of an intrinsic property of fermions, *spin*. In 1925 Goudsmidt and Uhlenbeck proposed the spin quantum number for the electron to allow the complete description of the hydrogen atom. If an electron is simply represented as a ball of spinning charge then in an atom, the charge is moving in a circular path around the nucleus and can be described classically as an Amp rean current loop [29]. All fermions, including protons, neutrons and electrons, possess a spin of ½. It is the property of spin that leads to the ability of the nucleus to act as a miniature bar magnet and undergo nuclear resonance.

In 1938, Isidor Rabi conducted the first measurements to yield accurate results on the nuclear magnetic moment by studying molecular beams of lithium [31, 32]. His work was of such importance to nuclear physics that he received the Nobel Prize in Physics in 1944. In 1946, Bloch and Purcell, working independently, first achieved nuclear magnetic resonance in condensed matter [33 – 35]. Felix Bloch and Edward Purcell shared the 1952 Nobel Prize in Physics for their contributions to NMR. The nuclear magnetic moment and concept of resonance is the foundation of all subsequent NMR experiments and has permitted the development of magnetic resonance imaging (MRI).

2.2 NMR Physics

2.2.1 The Atomic Nucleus

Magnetic Resonance Imaging (MRI) is an imaging method based upon the nuclear magnetic resonance (NMR) phenomenon first discovered in the 1930's. NMR can be observed in systems of nuclei that possess a magnetic moment as a result of angular momentum. When these nuclei are exposed to an external magnetic field, it is possible, through perturbation of the nuclei, to elucidate information about the chemical environment of those nuclei. This section will detail basic atomic structure and outline the physics that describe nuclear magnetic resonance and introduce the concepts of precession and relaxation.

The protons and neutrons of an atom are collectively known as nucleons. Electrons orbit the atomic nucleus in allowed shells or orbitals, with the number of orbitals increasing as the number of electrons around the nucleus increases.

Nuclear orbitals are occupied by nucleons (protons and neutrons) and are filled according to strict quantum mechanical rules that are analogous to the filling of atomic orbitals by electrons. The Pauli exclusion principle dictates that no two identical fermions (i.e. two protons or two neutrons) can occupy the same state. In nuclei, the lowest energy quantum state can be filled by only one nucleon, the next nucleon then occupies the next lowest energy state and so on. This occurs for both protons and neutrons. A consequence of this restriction is that nucleons experience a pairing force. In nuclei, the pairing force favours the coupling of nucleons so that their orbital angular momentum and spin angular momentum each add to zero. As a result, paired nucleons do not contribute to the net magnetic dipole moment. This pairing force allows the electromagnetic properties to be determined from only a few valence nucleons [36].

NMR occurs only in systems that possess a net angular momentum and therefore have a magnetic dipole moment. To understand why, it is necessary to explain the structure of the atom in more detail. Every nucleon can be labelled with the quantum numbers *l*, *s*, and *j*, corresponding to the orbital, spin and total angular momentum of each nucleon respectively. Nucleons are coupled together in nuclei so that in a given state the total angular momentum of a nucleus with n nucleons is the vector sum of the angular momenta of the individual nucleons. The total angular momentum of the nucleus is referred to as the *nuclear spin*, and is denoted by $\mathbf{I}$. $\mathbf{I}$ has the usual properties of quantum mechanical angular momentum vectors where $\mathbf{I}^2 = \hbar^2 \mathrm{I}(\mathrm{I}+1)$ and $\mathbf{I}_z = m\hbar$ $(m = -\mathrm{I}, -\mathrm{I}+1, \ldots, \mathrm{I})$. The nuclear spin and the magnetic dipole moment are related by

$$\boldsymbol{\mu} = \gamma \mathbf{I} \qquad (2.1)$$

where γ is the gyromagnetic ratio. For a proton γ = 2.675 x 10^8 $s^{-1}T^{-1}$ however this value varies from nucleus to nucleus as is shown in table 2.1 [37]. The nuclei in table 2.1 were chosen to represent some of the most commonly studied nuclei in MRI. Equation 2.1 shows that if $\mathbf{I}$ is zero, then the magnetic dipole moment must also be identically zero. As will be shown shortly, only a nucleus with a nonzero magnetic dipole moment will experience nuclear magnetic resonance.

Nucleus	Nuclear Spin **I**	γ (MHz/T)	Isotopic Abundance %
^{1}H	1/2	42.6	99.98
^{13}C	1/2	10.7	1.108
^{17}O	5/2	5.8	0.037
^{19}F	1/2	40.0	100
^{23}Na	3/2	11.3	100
^{31}P	1/2	16.7	100

Table 2.1: Nuclear spin, gyromagnetic ratio and natural isotopic abundance of nuclei commonly studied using MRI.

The balance between the number of protons and neutrons in an atom determines the angular momentum of the nucleus. If a nucleus contains either unpaired protons or unpaired neutrons or both then it will have a net non-zero spin and thus a non-zero magnetic moment. In hydrogen (^{1}H), an odd-Z nucleus, where Z is the number of protons, the nucleus contains one proton whose spin angular momentum is s = ±½, where ± depends on the state the nucleus is in. For a particle of spin, s, its projection onto the *z* axis can take on one of several values, labelled m_S (m_S = -s, -s + 1,..., +s). In the ground state of ^{1}H, m_S = +½, and as it is the sole nucleon, l = 0, so $\mathbf{I} = l + s$ = ½. In even-Z, even-N nuclei, where N is the number of neutrons, the pairing force causes nucleons to couple into spin-0 pairs, giving a total $\mathbf{I}$ = 0. Helium (^{4}He) is an example of this. Its nucleus is composed of two protons and two neutrons. The two protons couple in a spin-0 pair so $\mathbf{I}_P = 0$ as do the two neutrons, so $\mathbf{I}_N = 0$. The resultant sum, or nuclear spin, is $\mathbf{I} = \mathbf{I}_P + \mathbf{I}_N = 0$ [36]. For each nucleon in the two pairs, the exclusion principle causes one nucleon to assume m_S = +½ and the other nucleon to assume m_S = -½. Therefore, ^{4}He does not have a magnetic dipole moment and does not exhibit NMR.

MRI takes advantage of the natural abundance of specific biologically relevant nuclei. Hydrogen, ^{1}H, is of particular interest because 60% of the human body is composed of water. Moreover, when fat is considered, nearly two-thirds of all atoms in the human body are hydrogen [38, 39]. Some of the

other biologically important nuclei that are commonly studied include ^{13}C, ^{17}O, ^{19}F, ^{23}Na and ^{31}P.

2.2.2 Precession in a Magnetic Field

The Irish physicist Joseph Larmor demonstrated in 1897 that if an aligning force were applied to a spinning object, then the object would undergo precession. When a spinning, charged particle, such as a proton, is placed in a magnetic field, the effect is similar to the precession observed in a child's top as it slows down. As explained in the previous section, the nucleus of ^{1}H has a nonzero nuclear spin and magnetic dipole moment. Therefore the hydrogen nucleus will precess in an external magnetic field analogously to the precession of a top in a gravitational field as shown below in figure 2.1.

For an external magnetic field $\mathbf{H}$, a torque will be produced on the magnetic moment $\boldsymbol{\mu}$ according to $\boldsymbol{\mu}\times\mathbf{H}$. To determine the equation of motion of the magnetic moment within the external field, the time rate of change of the angular momentum $\mathbf{I}$ is equated to the torque.

$$\frac{d\mathbf{I}}{dt} = \boldsymbol{\mu}\times\mathbf{H} \qquad (2.2)$$

Now $\mathbf{I}$ can be eliminated using equation 2.1 to yield

$$\frac{d\boldsymbol{\mu}}{dt} = \boldsymbol{\mu}\times(\gamma\mathbf{H}) \qquad (2.3)$$

Equation 2.3 holds whether $\mathbf{H}$ is static or varies with time [40]. It also shows that the changes in $\boldsymbol{\mu}$ are perpendicular to the directions of the externally applied magnetic field and the magnetic dipole moment. The angle θ is defined as the angle between the magnetic moment and the applied magnetic field, and does not change with time. If $\mathbf{H}$ is static then $\boldsymbol{\mu}$ precesses about $\mathbf{H}$ such that it sweeps out a cone whose central axis is collinear with $\mathbf{H}$. In clinical MRI, the applied field is static and as such, the following derivation of the equation of motion will assume a static, external magnetic field. The equation of motion, equation 2.3, has been derived in the laboratory frame of reference. Because

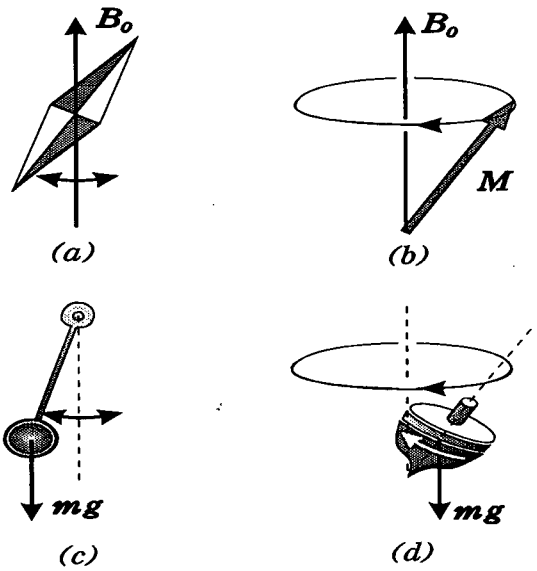

Figure 2.1: The motion of μ = M about the applied magnetic field B_0 in (b) can be compared to that of a compass needle (a). It is analogous to a spinning top (d) and a pendulum (c), except the gravitational field in (c) and (d) is replaced by a magnetic filed in (a) and (b). (reproduced with permission from S. Xiang)

the system of interest is rotating around a constant, applied magnetic field, it is more useful to transform the equation of motion to a reference frame that rotates at the same rate as the precessing nucleus. The axes transform to $z \rightarrow z$ (the axis of rotation), $x \rightarrow x'$ and $y \rightarrow y'$. The equation of motion for $\boldsymbol{\mu}$ can be rewritten with the addition of an undetermined angular velocity $\boldsymbol{\omega}$.

$$\frac{\delta \boldsymbol{\mu}}{\delta t} = \boldsymbol{\mu} \times (\gamma \mathbf{H} + \boldsymbol{\omega}) \tag{2.4}$$

The equation of motion is the same as that in the laboratory reference frame when an effective field, $\mathbf{H}_e$, is introduced such that

$$\mathbf{H}_e = \mathbf{H} + \frac{\boldsymbol{\omega}}{\gamma} \tag{2.5}$$

In a static external magnetic field applied along the z-axis, $\mathbf{H} = H_0\hat{\mathbf{k}}$, if ω is selected such that $\mathbf{H}_e = 0$, then

$$\boldsymbol{\omega}_0 = -\gamma H_0 \hat{\mathbf{k}} \tag{2.6}$$

From Equation 2.6 $\boldsymbol{\mu}$ rotates at an angular velocity $\boldsymbol{\omega}_0 = -\gamma H_0 \hat{\mathbf{k}}$ with respect to the laboratory frame [40]. The frequency γH_0 is known as the resonant (or

'natural') or *Larmor* frequency. The nucleus precesses at its resonant frequency, determined linearly by the strength of the external magnetic field and the gyromagnetic ratio of the nucleus. Using table 2.1, the Larmor frequency of a ^1H nucleus in a 1 T field is calculated to be 42.6 MHz.

2.2.3 Relaxation Times

The total magnetization, **M**, of a sample is defined as the sum of the vectors of the individual magnetic dipole moments in a unit volume of the medium or $\mathbf{M} = N\boldsymbol{\mu}$. This allows equation 2.3 to be rewritten as

$$\frac{d\mathbf{M}}{dt} = \gamma \mathbf{M} \times \mathbf{H} \tag{2.7}$$

Assuming that the applied magnetic field is along the positive *z* axis, or $\mathbf{H} = H_0\hat{\mathbf{k}}$, then at thermal equilibrium the three components of the magnetization will be

$$M_X = 0; \quad M_Y = 0; \tag{2.8}$$

and

$$M_Z = M_0 = \chi_0 H_0 = C\frac{H_0}{T} \tag{2.9}$$

Here C is the Curie constant, $C = N\mu^2/3k_B$, χ_0 is the static magnetic susceptibility, T is the temperature and k_B is the Boltzmann constant. For simplicity, a system is considered which only contains nuclei of spin ½. The number of nuclei in each of the two states $m_S = +½$ and $m_S = -½$, are described by Boltzmann statistics. The sample's net magnetization will be equal to the population difference times the magnetic dipole moment. The populations of the $m_S = +½$ and $m_S = -½$ energy levels are represented by N_+ and N_- respectively. Therefore $\mathbf{M}_Z = (N_+ - N_-)\boldsymbol{\mu}$ and the energy difference between levels is $2\mu H_0$. The ratio of the two populations at thermal equilibrium is

$$\left(\frac{N_-}{N_+}\right)_0 = \exp\left(\frac{2\mu B_o}{k_B T}\right) \tag{2.10}$$

The equilibrium magnetization is given by

$$M_0 = N\mu \tanh\left(\frac{\mu B}{k_B T}\right)\hat{\mathbf{k}} \tag{2.11}$$

This will be oriented along z. If the system is not in equilibrium then it is assumed that it will approach equilibrium at a rate proportional to its difference from the equilibrium magnetization.

$$\frac{dM_Z}{dt} = \frac{M_0 - M_Z}{T_1} \tag{2.12}$$

T_1 is known as the longitudinal relaxation time or the spin-lattice relaxation time because it is the time it takes for the spins to transfer energy to the lattice. M_0 is the thermal equilibrium magnetization. In thermal equilibrium the nuclear levels will have the same relative populations as does the lattice [40]. T_1 is a characteristic time that is associated with the approach to thermal equilibrium.

Initially, an unmagnetized sample will have a net magnetization of zero along any coordinate direction. This is because the individual magnetic dipoles point in random directions in the absence of an external magnetic field.

Just before and immediately after the unmagnetized sample experiences the externally applied field, the populations of N_+ and N_- will be equal, as appropriate to thermal equilibrium in the absence of an external field. In order to establish a new equilibrium in the applied field some of the spins are reversed. The individual nuclei align their magnetic moments with the applied field. They will align either parallel (low energy configuration) or anti-parallel (high energy configuration). The thermal equilibrium value of the magnetization is due to the population difference between these two configurations. Boltzmann statistics predict that slightly more nuclei will align parallel to the applied field than those that align anti-parallel to the field. Integrating equation 2.12 yields

$$\int_0^{M_Z} \frac{dM_Z}{M_0 - M_Z} = \frac{1}{T_1}\int_0^t dt \tag{2.13}$$

The magnetization will increase from $M_Z = 0$ to $M_Z = M_0$, its thermal equilibrium value according to

$$M(t) = M_0(1 - \exp\{-t/T_1\}) \tag{2.14}$$

Therefore T_1 is the time constant that characterizes the time needed to magnetize an unmagnetized sample. The magnetization asymptotically

approaches its maximum value M_0 at time t >> T_1. At time t = T_1 the magnetization has achieved 63 % of its equilibrium value in the external magnetic field. The magnetic energy $-\mathbf{M}\cdot\mathbf{H}$ decreases as M_Z approaches the equilibrium value. By combining equation 2.12 with the equation for the driving of **M** by the torque, equation 2.7, the result is

$$\frac{dM_Z}{dt} = \frac{M_0 - M_Z}{T_1} + \gamma(\mathbf{M}\times\mathbf{H})_Z \qquad (2.15)$$

At thermal equilibrium in a static magnetic field applied along *z* the net magnetization **M** will align with $\mathbf{H}$. Therefore any transverse components of **M** must vanish in equilibrium. Because the spins align with the applied magnetic field, the transverse components must approach $M_{XY} = 0$ at t = ∞. The evolution of the magnetizations, M_X and M_Y, are also expressed in the form of differential equations that are written as

$$\frac{dM_X}{dt} = -\frac{M_X}{T_2} + \gamma(\mathbf{M}\times\mathbf{H})_X \qquad (2.16)$$

$$\frac{dM_Y}{dt} = -\frac{M_Y}{T_2} + \gamma(\mathbf{M}\times\mathbf{H})_Y \qquad (2.17)$$

T_2 is known as the transverse relaxation time and is distinct from T_1 because it involves interactions occurring between different spins. For two protons near each other, the local magnetic field from one proton affects the other proton and vice versa. This variation in the magnetic field causes individual protons to experience different magnetic fields leading to very small variations in the Larmor frequency of each. The average Larmor frequency remains the same, however the frequencies of the individual protons vary randomly because they can move throughout the sample. The result is that the magnetizations of the individual spins become out of phase, or dephase, which causes a decrease in the net magnetization. T_2 is the rate at which energy is dissipated through spin-spin interactions. Equations 2.15 –2.17 were first proposed by Felix Bloch and are hence known as the Bloch equations [33, 34].

If the sample experiences a transient magnetic field, perpendicular to the static field applied along *z*, then a component of the magnetization vector will be tipped into the *x-y* plane. When this applied field is removed, the transverse and longitudinal magnetizations will return to their equilibrium values.

For the case where $M_X(0) = 0$, $M_Y(0) = M_{XY}^0$, and $M_Z(0) = M_Z^0$ and a field is applied for a time t, the return to equilibrium is given by

$$M_X(t) = M_{XY}^0 \sin\omega_0 t \cdot \exp\{-t/T_2\} \tag{2.18}$$

$$M_Y(t) = M_{XY}^0 \cos\omega_0 t \cdot \exp\{-t/T_2\} \tag{2.19}$$

$$M_Z(t) = M_0 + (M_Z^0 - M_0) \cdot \exp\{-t/T_1\} \tag{2.20}$$

If $\mathbf{H}$ is along *z* then the magnetic energy will not change as M_X or M_Y changes.

2.3 Detection of an NMR Signal

The previous section outlined the equations of motion of a magnetic dipole when it is exposed to a static external magnetic field. It also provided an explanation of the basis of the fundamental parameters commonly studied in magnetic resonance imaging, the T_1 and T_2 relaxation times. Now that the physics of relaxation has been described, it is possible to explain how an NMR signal is acquired when the net magnetization of a sample in static, external magnetic field is perturbed.

To understand how a signal is generated using MRI, the sample is assumed to be in an external magnetic field $\mathbf{H}$, applied along *z*. The net magnetization, **M**, at equilibrium precesses about *z*. By applying a short duration, strong radiofrequency (RF) pulse perpendicular to the static field $\mathbf{H}$, **M** can be tipped away from its equilibrium orientation. In MRI, the pulse is specifically selected to occur at the Larmor frequency of the nuclei of interest. These nuclei will resonate and their net magnetization will try to align with the direction of the applied pulse. The angle that the magnetization is tipped away from *z* is known as the flip angle and is defined by

$$\alpha = \omega_1 \tau \tag{2.21}$$

Here α is the flip angle, ω_1 is the Larmor frequency in the effective field, and τ is the duration of the RF pulse. Clinical MRI systems often employ magnetic fields with strengths ranging from 0.5 T – 1.5 T. As a result, the Larmor frequency is in the radio frequency range. The pulses are therefore referred to as 'RF pulses' or 'excitation pulses' because they are the source of the signal that is to be detected.

If the RF pulse is applied along the *x* direction for a time τ, then immediately following the application of the RF pulse, at t = 0, the magnetization, **M**, is aligned along *yz* plane. In the special case when τ is chosen such that the $\alpha = 90°$, there will be no magnetization along *z* because M_0 is rotated so that it falls exactly onto the transverse plane, along the *y* axis. When $\alpha = 180°$, the magnetization is inverted to point along $-z$ at t = 0. By defining M_Z^0 and M_{XY}^0 as the components of **M** in the longitudinal and transverse planes at t = 0, the Bloch equations can be solved as

$$M_Z(t) = M_0 + (M_Z^0 - M_0)e^{-t/T_1} \tag{2.22}$$

$$M_{XY}(t) = M_{XY}^0 e^{-t/T_2} \cdot e^{i\cdot\omega_0 t} \tag{2.23}$$

Equation 2.23 indicates that a change in phase occurs in the transverse component as time increases. Figure 2.2 illustrates the change in M_Z, M_X, and M_Y as a function of time for a pulse applied along *x*.

The explanation of relaxation above shows that as t → ∞, M_{XY} will decay with a time constant T_2 while M_Z will increase exponentially with a time constant of T_1. Equations 2.22 and 2.23 represent time varying magnetizations. From Faraday's Law, a time-varying magnetic field will induce a current in a coil of conducting wire because the magnetic flux through the wire will change. To detect an NMR signal a coil is placed along *x* or *y* and the current induced in the coil due to the changed magnetization is measured. The induced signal decays because of the loss of magnetization M_{XY}, and the resulting curve is known as a free induction decay (FID). Using induction was the method first discovered by

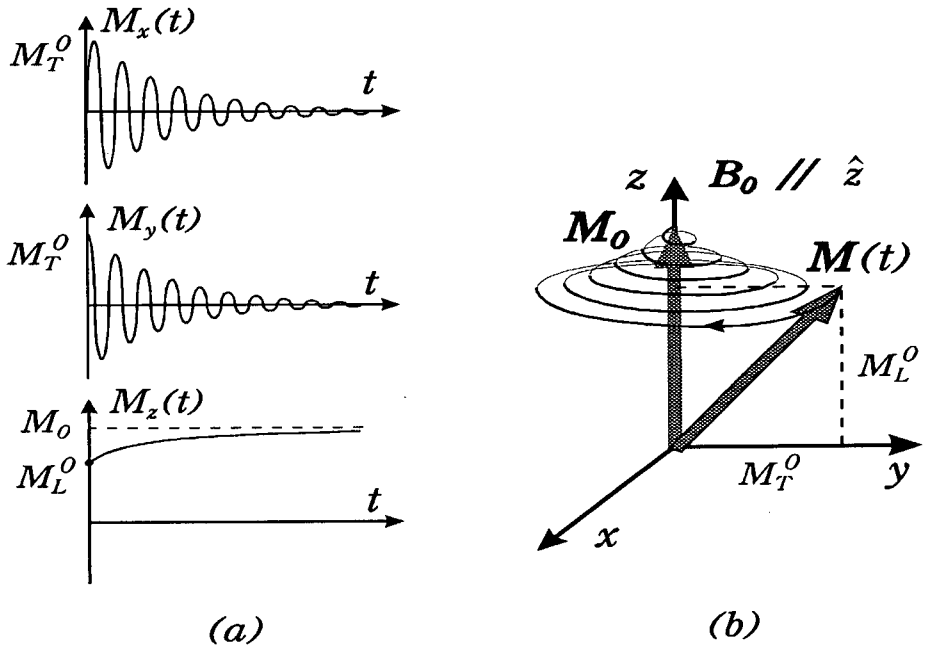

Figure 2.2: Time evolution of the magnetization vector **M** *(a)* M_x, M_y, *and* M_z *as functions of time. (b) The motion of* **M** *vector in 3D. The* **M** *vector undergoes a Larmor precession with* $\omega_0 = \gamma H_0$ ($H_0 = B_0$ *as well as* T_1 *and* T_2 *relaxations, and eventually reaches its thermal equilibrium state* $\mathbf{M}_0$. *(reproduced with permission from S. Xiang)*

Bloch and is the basis of current clinical MRI [33, 34]. Purcell utilized a method based on the absorption of energy when the frequency of an applied current through a coil matched the resonant frequency of the sample [35].

Normally the coil that is used to receive the FID is also the same coil used to transmit the excitation pulse to the sample or patient. If the coil is aligned with x, and the excitation pulse is along x, then at t = 0, M_{XY} will be aligned with y, so no signal will be detected. At a time t_1, the precessing protons will have rotated 90° and have aligned with x generating a signal. After a further 90° rotation, at time $t = t_2$, the magnetization will align along $-y$, again yielding no signal. At t_3, after another 90°, they will point along $-x$, so the signal will be opposite in sign in the coil. Therefore the received signal varies sinusoidally in time. However, due to interactions between different nuclei and external field inhomogeneties, the precessing protons begin to dephase and immediately following the excitation pulse at t = 0. As the protons precess and relax, the magnitude of the signal decreases with time creating the FID. This is shown in figure 2.2.

The FID is described by an exponentially decaying sinusoid whose time constant is T_2^*. T_2^* is dependent on the spin-spin interactions that lead to T_2 relaxation but is also caused by inhomogeneties in the static magnetic field. These inhomogeneties contribute to the different local magnetic environments experienced by individual nuclei and therefore also lead to variation in the resonant frequencies. Therefore, $T_2^* \leq T_2$ and is equivalent to T_2 only when the external field is uniform and homogeneous. Losses in the detected signal due to T_2^* effects can be corrected, as will be explained next.

2.4 Spin Echoes

T_2^* relaxation creates a tremendous difficulty in determining the actual T_2 of the sample because T_2^* relaxation occurs faster than T_2 relaxation. Fortunately, it is possible to correct for the field inhomogeneities that contribute to T_2^*. In 1950, Hahn discovered that an RF pulse applied to a group of spins following a FID would result in a second FID [41]. His discovery was a cornerstone in the development of the pulsed methods in NMR. It led to a better understanding into the resonance phenomenon and is the basis of many conventional MRI methods used today.

Hahn's original experiment employed a second 90° pulse applied a time τ after the initial 90° pulse, which led to generation of a second FID. The origin of the spin echo is easier to visualize however when 180° pulses are used after the excitation pulse. 180° refocusing pulses were first used to generate echoes in 1954 by Carr and Purcell [42]. The 180° refocussing pulses are effective at correcting for losses in M_{XY} due to external field inhomogeneities, or T_2^*, but do not correct losses arising from spin-spin interactions, T_2.

The rotating frame of reference is again used to describe the spin echo. Again the axes x' and y' appear stationary. The net magnetization, M_{XY}, does not precess about z in this frame, but points in the same direction that it was tipped onto by the excitation pulse. Assuming that an initial 90° pulse is applied along x', and the static field is pointed along z, then M_0 is tipped from its

equilibrium position onto y'. In other words, at t = 0, $M_{XY} = M_0 = M_Y$. The spins in the *x-y* plane will immediately begin to dephase after cessation of the excitation pulse due to magnetic field inhomogeneities and spin-spin interactions. The net magnetization vector decreases in magnitude due to dephasing but its direction remains along *y'*. While most of the spins precess at ω_0, some will precess slightly faster or slower than the Larmor frequency. After a time τ, $M_{XY} = M_Y(\tau)$ and is less than its initial value by an amount given by equation 2.23. If a 180° pulse is applied at time τ along *y'*, the phase of each spin will invert 180° about *y'* but allows dephasing to continue. After inversion, further dephasing causes the spins to realign after a second period of time τ along *x'*. As the spins come back into phase, the net magnetization increases until all spins are in phase. At t = 2τ the amplitude of M_{XY} is a maximum. Another FID occurs because of the difference in Larmor frequencies. Therefore the spins dephase again. This second signal is known as the spin echo. The sequence of RF pulses used to generate the echo at time 2τ is denoted by $90^0_{x'} - \tau - 180^0_{y'} - \tau - echo$. This sequence of pulses is known as the CPMG sequence (Carr-Purcell-Meiboom-Gill) and is illustrated in figure 2.3 [43].

The original sequence proposed by Carr and Purcell (CP) differs from the CPMG by the axis about which the 180° pulse is applied. figure 2.4 shows the variation between the sequences. Application of the 180° pulse about *y'* corrects for small errors in the RF pulse that would normally accumulate if the pulse was applied about the *x'* axis. In figure 2.4A, the CP sequence, each rotation of the dephased spins about the *x'* axis results in a small loss of signal at each echo because the RF pulse is not exactly 180°. Some spins do not undergo a complete 180° rotation and end up outside of the x-y plane. Rotations of 180° around the *y'* axis, such as those shown in figure 2.4B, correct for losses that are

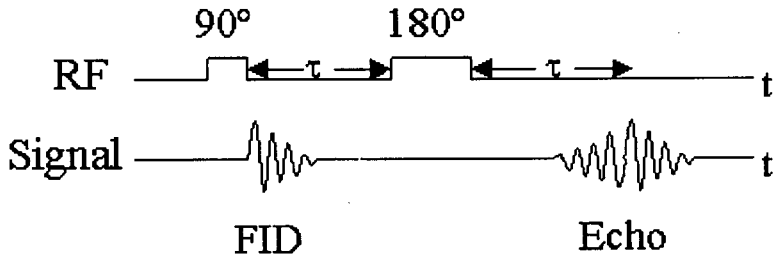

Figure 2.3: A 90-τ-180-τ-echo sequence showing the timing of the 90° and 180° pulses. Following the 90° pulse, the signal forms a free induction decay due to T_2^* effects. After a time τ, a 180° pulse is applied, causing an echo at time 2τ. Repeated 180° pulses forms an echo train, that decays with time constant T_2.

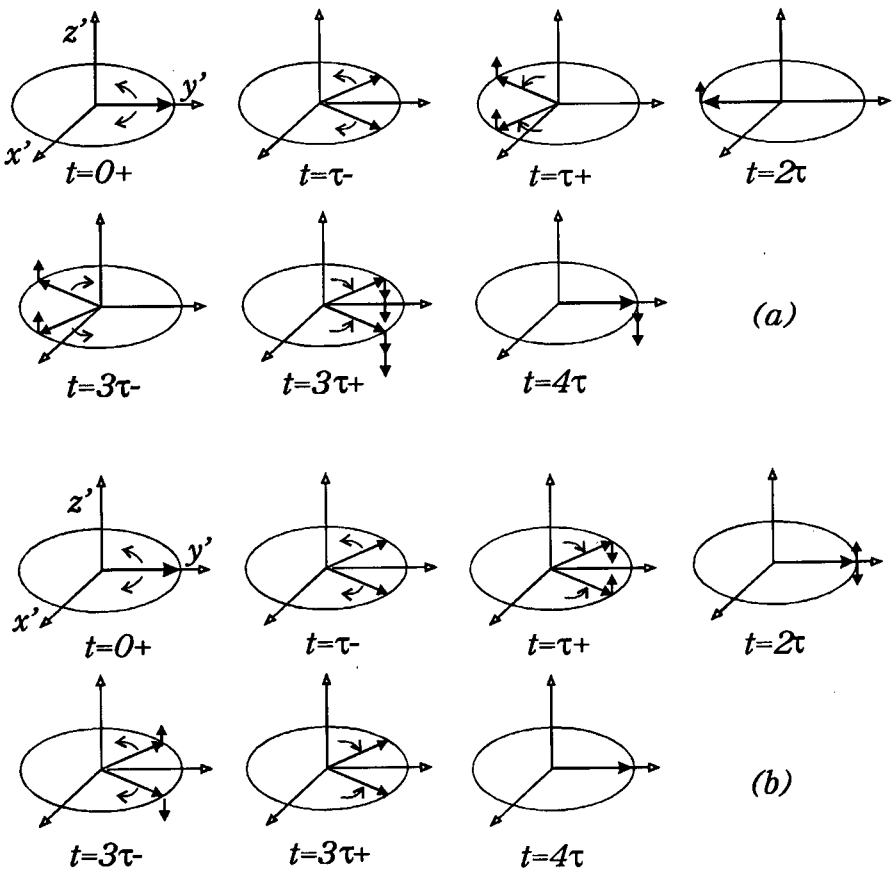

Figure 2.4: RF error accumulation in A) a CP sequence and error correction in B) a CPMG sequence. The 180° rotation about y' corrects errors due to imperfect RF pulses at every other echo. (reproduced with permission from S. Xiang)

caused by imperfect 180° pulse on every other pulse. At time t = 2τ, the initial 180° pulse is imperfect and causes some spins to end up in y-z plane. However, this error cancels out the error at the next echo, at t = 4τ, which leads to complete rephasing at the second echo.

In a conventional spin echo (CSE) experiment a series of 180° pulses are used with each pulse separated by 2τ and each generates an echo at time τ after the refocussing pulse. This results in a train of echoes, each with successively smaller amplitudes. The decrease in amplitude of each echo is due to T_2 relaxation. Thus the envelope formed from the peak amplitude of each echo will decrease with a time constant T_2, while the signal following each echo decreases in amplitude according to T_2^*. The relationship between T_2^* and the FID is illustrated in figure 2.5.

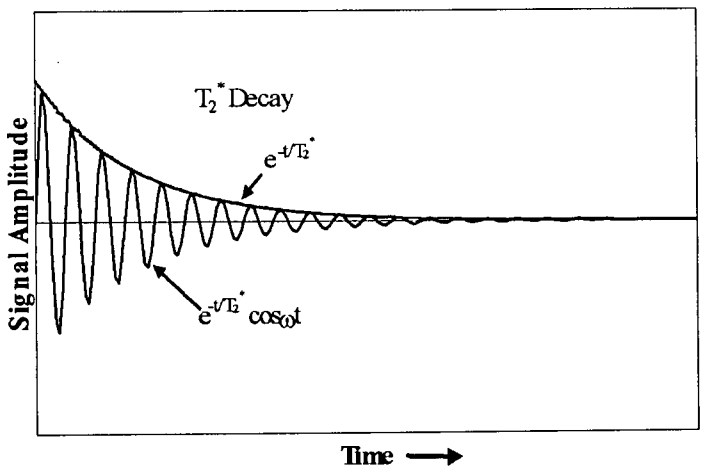

Figure 2.5: A single free induction decay showing the exponentially decaying sinusoid and its envelope. The envelope decays with a time constant of T_2^*.

2.5 Pulse Sequences

To understand the basis of MRI images an understanding of how pulse sequences use the field gradients and RF pulses to spatially encode information is necessary. This section will introduce MRI pulse sequences and basic parameters such as repetition time, TR, and echo spacing, TE.

MRI is an imaging modality where spatial information from a patient can be mapped with tremendous resolution. MRI scanners use a main magnet to

generate a large magnetic field, H_0, of 0.5 – 1.5 T along *z*. This main field is designed to be of homogeneous intensity within the region to be imaged. To create a map of the NMR signal arising from protons within a specific area of the body it is necessary to spatially encode the received signal. Spatial encoding can be accomplished in several ways but the simplest and most commonly used method is by applying three distinct localization methods.

Spatial encoding is accomplished through introducing small magnetic field gradients superimposed on the main field. The gradients are oriented along *x*, *y*, and *z*, however the magnetic fields associated with them remain directed along the main magnetic field's direction. These gradients are small in comparison with the main field, with a maximum strength of approximately 10 mT m^{-1}. The gradients typically vary linearly with distance. The result is a spatial variation in the field experienced by the sample to be mapped, and therefore a spatial variation in the Larmor frequency of individual nuclei.

In the simplest case, the gradients are used in three steps of localization. The first gradient, G_z, is called the slice-select gradient. In *z* localization, a constant gradient is applied along *z* causing a shift in the Larmor frequency as the slice of interest is moved along *z*. The RF pulse can be selected to match a range of Larmor frequencies, known as the bandwidth, which will only cause those protons within a specific location along *z* to resonate. The RF pulse is applied at the same time that the G_Z gradient is turned on. For a 90° RF pulse, the net magnetization in this slice will tip onto the transverse plane while protons outside the slice will not resonate because their Larmor frequencies differ from the RF pulse. As only a thin slice of the body is excited this is known as slice selection.

Once G_Z and the RF pulse select a transverse plane to spatially encode, the final two gradients G_X and G_Y can be activated. G_X and G_Y are also known as frequency encoding and phase encoding gradients respectively. This distinction is merely a convention and can be reversed. The spatial information is elucidated through the use of the Fourier Transform (FT). The FT of a signal with multiple frequency components provides information on how much each

component has contributed to the total signal as well as the phase relation between components. In MRI, the selected slice is again subjected to gradients along *x* and *y*, resulting in spatially varying Larmor frequencies in these additional directions. The frequency encoding results in different Larmor frequencies depending on the location of the spins along *x*.

Phase encoding is accomplished through the third gradient, G_Y. When G_Y is applied the spins accumulate a phase rotation dependent upon their *y* location. If G_Y is applied to cause a phase difference in the spins, followed by application of G_X for x localization, then the projection of spins within the slice onto the x-axis is affected. By repeating this process for different G_Y strengths, a set of x projections can be acquired. Differences in spatial position up and down are reflected in phase values, while differences in spatial location left to right is given by the frequency value. The use of the G_X and G_Y gradients therefore permit the spatial distribution of a slice to be mapped according to small variations in the frequency and phase of different spins. Applying a 2-dimensional FT (2DFT) to this set of projections then yields the two-dimensional MR image.

The MR image that is acquired is a three-dimensional data set because of the finite thickness of the slice that is selected with G_Z. Typical slice thickness is on the order of 1 – 10 mm. Localization in three directions results in a dataset of small volume elements, or voxels. In 2-dimensional images, only information in *x* and *y* is relevant and the corresponding picture elements are called pixels. For the remainder of this thesis, pixels and voxels are used interchangeably but it should be noted that all images acquired through MRI are 3-dimensional datasets. Each pixel on the 2DFT is a vector field, and can be represented as a complex number, with real and imaginary components. Therefore, it is possible to construct two separate images, one real and one imaginary, from a 2DFT dataset. Within each pixel, the intensity is mapped onto a grey scale, where the lightest shade corresponds to the greatest signal received.

The sequence of steps involved in selecting a slice and encoding spatial information and receiving the signal generated is referred to as the pulse sequence. Pulse sequences are represented using timing diagrams illustrating

when the RF and gradient pulses are applied relative to each other. The sequence is shown as a series of lines, indicating the RF pulse, the three gradient pulses, G_X, G_Y, and G_Z, and the received signal. The RF pulse is indicated by either a Gaussian or sinc lineshape or by a boxcar. In the case of a boxcar, a 90° and 180° pulse are given different widths. In both cases, the axis

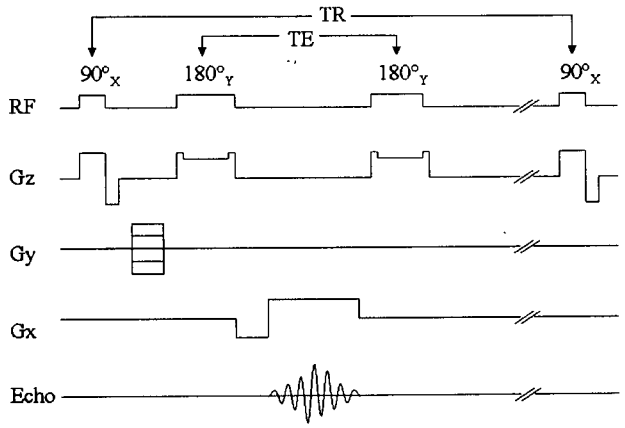

Figure 2.6: Conventional spin echo (CSE) timing diagram illustrating the 3 field gradients, G_Z, G_Y, and G_X. The 180° pulses are separated by the echo time, TE, and the time between successive 90° excitation pulses is the repetition time, TR.

along which the excitation pulse is applied is subscripted next to the tip angle. The gradient pulses are denoted by a boxcar shape because ideally the gradients are turned on and off very quickly and have a constant amplitude while they are activated. A typical slew rate of a 1.5 T commercial scanner is on the order of 120 mT/m/ms. A CSE timing diagram is shown in figure 2.6.

As stated earlier, the phase encoding step is often repeated to gather different phase encoded *x* projections. For example, if only one phase encoding is performed for each excitation pulse delivered to a slice, and 128 phase encoding steps represents a complete *x* projections, then the excitation pulse must be repeated 128 times. Each time the excitation pulse is applied the gradient G_Y is changed slightly. The time between the successive excitation pulses is called the repetition time, TR.

In a CPMG CSE sequence, the T_2 characteristics of the sample can be found by measuring the decay of the signal acquired from multiple spin echoes. After the excitation pulse, a refocussing pulse (180°) is applied a time τ later. This produces an echo at time 2τ. A second 180° pulse is applied at 3τ, generating a second echo at 4τ. This is repeated for n echoes, where the 180° pulse is applied at $(2n + 1)\tau$ with successive echoes received at $(2n + 2)\tau$. Between each refocussing pulse and the echo it generates, G_Y is activated to select a specific phase encoding by changing the amplitude of the G_Y pulse. G_X is turned on before the echo such that it reaches the maximum amplitude in the middle of the G_X gradient. G_X is also known as the read-out gradient because the NMR signal is acquired while G_X is active. The time between successive echoes is called the echo spacing, TE. TE is related to τ by $TE = 2\tau$ and is typically much shorter than TR.

Because data collection occurs when the magnetization is tipped into the transverse plane, the excitation pulses must be spaced far enough apart to allow a significant amount of T_1 relaxation to occur, so TR >> T_1. If this does not occur, the second excitation pulse will only tip a small proportion of M_0 back onto the transverse plane. New pulse sequence methods utilize the dead time between the acquisition of the final echo and the next excitation pulse to collect other slices, or collect multiple lines in the phase encoding direction with a single excitation pulse.

2.6 k-space

In a typical MRI sequence, the amount of phase encoding varies over a specific number of steps. For each step the phase encoding gradient is increased or decreased slightly, after which the frequency encoding gradient is applied. It is necessary to do many phase encoding steps in order to complete a data acquisition, and the complete set is referred to as the data space or data matrix, and has dimensions of *x* by *y*. A 256 x 128 data or acquisition matrix corresponds to 256 frequency encoding steps, or the number of times the data is sampled during read-out, and 128 phase encoding steps. Each of the 256 points

in one of the 128 lines of the data matrix is a sample of the echo. The data matrix is related to the MR image through application of a 2DFT. *k*-space is derived from the data matrix and like an MR image is complex. It therefore contains both real and imaginary components and each of these components can be separated and shown as two separate images. The real and imaginary matrices are the raw data matrices. *k*-space is described by two coordinate

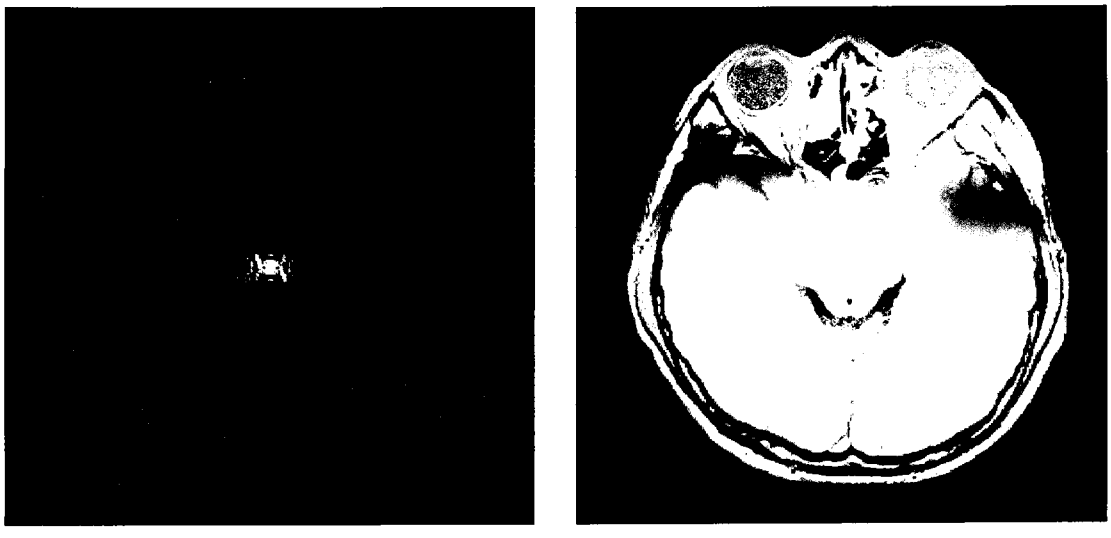

(a) (b)

Figure 2.7: The raw data matrix and the image constitute a 2D Fourier transform pair. Only magnitude data are presented although both data sets are complex. (a) The phase encoded induction signals written as a raw data matrix. (b) The image reconstructed by a 2DFT of the raw data matrix. (reproduced with permission from S. Xiang)

directions, k_X and k_Y. Figure 2.7 shows a raw data matrix and the resulting MR image after application of a 2DFT.

In a CSE image, each line of phase encoding is collected individually, so k_Y corresponds to a specific phase encoding signal. *k*-space is collected starting in the center of the data matrix. For a matrix with 128 phase encoding steps, the zero-step (no phase-encoding) is in the middle of *k*-space and it is incremented outwards, alternately positive and negative from –63 and $k_Y = +64$. This is the same in the frequency encoding direction, k_X. For 256 frequency encoding steps, the center of k-space is 0 and the outside goes from –127 to +128. This is

because the maximum signal occurs when there is no phase encoding or frequency encoding gradients applied.

By denoting the spins at a particular location, **r**, as the spin density, $\rho(\mathbf{r})$, then the 2D Fourier relationship between the signal, S(k), and spin density is given by

$$\rho(\mathbf{r}) = \iiint S(\mathbf{k}) \exp\{-i\mathbf{k}\cdot\mathbf{r}\} d\mathbf{k} \qquad (2.24)$$

For the 2D FT used in image construction of 2D MR images, equation 2.24 reduces to a double integral that is integrated over k_X and k_Y. Equation 2.24 is known as the fundamental imaging equation. The relationship between the field gradients, G_X and G_Y, and the axes of k-space, k_X and k_Y is given by

$$k_X = \gamma G_X t \qquad (2.25)$$

$$k_Y = \gamma G_Y \Delta t \qquad (2.26)$$

Equation 2.26 shows that when G_Y is applied for a short time Δt, there is a shift in the position along k_Y. In a CSE this is followed by application of G_X for a time t, which samples the data across k_X on the line of *k*-space specified by G_Y. The movement in *k*-space is known as the trajectory of the data acquisition. The speed with which each of these movements in *k*-space occurs is dependent upon the size of the individual gradients. Early MR imaging techniques acquired data in *k*-space at a single row for each TR, where k_Y was incremented successively. New techniques allow for multiple lines of *k*-space to be acquired per TR and can also allow for alternative trajectories to be acquired, such as spiral imaging.

Examining the timing diagram of a CSE sequence, as in figure *2.5*, slice selection is initially performed to excite a specific portion of the body. Because no gradients have been applied yet, the matrix is positioned at the center of *k*-space ($k_X = k_Y = 0$). The phase encoding gradient is then applied to select a line, k_Y in k-space that is to be filled. The readout or frequency encoding gradient is applied for a time t, which samples the echo received, filling the specified line k_Y. Normally, the readout gradient is preceded by a negative pulse with respect to the main readout pulse and applied for half the time of the positive readout gradient. This causes the position in *k*-space to shift to the far left. When

acquisition begins with the positive readout pulse, the maximum signal received will occur halfway across at *k*-space at $k_X = 0$. In the next TR, slice selection occurs again, and this time a new phase encoding level is applied, so that a new line in *k*-space is acquired.

Once the data has been acquired into the data matrix, application of the 2DFT turns the information into a useable MR image. The resolution of this image is dependent upon the number of phase-encoding and frequency-encoding steps performed during the pulse sequence. Because of the importance of minimizing patient time within the MR scanner, a compromise must be made between acquiring data of sufficient resolution in a minimal amount of time. A second tradeoff must be made because increased resolution comes at the expense of a decrease in the signal-to-noise ratio (SNR). This is due to higher resolution images corresponding to smaller voxels in the acquisition matrix. Increasing the number of voxels (increase in resolution) often leads to performing more phase encoding steps, thereby increasing acquisition time. Furthermore, if the signal is acquired from a smaller region, the number of protons available to contribute to the signal within that region is decreased. Methods exist to increase SNR such as signal averaging. In signal averaging, the same line of k-space is acquired n times. Noise fluctuates in amplitude randomly but the signal does not. As a result, by adding together multiple signals from the same location and averaging the signal, the noise will be diminished.

Once a suitable compromise in terms of SNR, resolution and acquisition time has been achieved, the MR pulse sequence is applied to the patient. The data can then be analyzed to extract useful information about the relaxation properties of the tissue of interest and any biological or chemical differences that may exist.

Chapter 3: Materials and Methods

3.1 Introduction

To study the effect of a variable echo spacing, two sets of experiments were conducted. In the first set a group of healthy volunteers were imaged using a series of different pulse sequences that utilized different combinations of echo spacings. The second set of experiments employed a set of water-based agarose phantoms designed to mimic the T_2 relaxation characteristics expected from cerebral tissue containing MS lesions. This chapter will provide an overview of the samples studied and the MRI pulse sequences and parameters used. It will also detail the relaxation analysis method, non-negative least squares, which was used to generate the T_2 distributions presented in chapters 4 and 5.

3.2 Human Brain

3.2.1 Patient Information

Ten normal volunteers were imaged, three men and seven women, mean age 27.4 years, ranging from 23 to 52 years. The volunteers were healthy and had no previous history of neurological dysfunction. All volunteers provided informed consent prior to participation in the study.

3.2.2 Regions of Interest

All volunteers were scanned in a transverse (or axial) plane through the genu and splenium of the corpus callosum. In this plane, a total of eight structures, four white matter and four gray matter, were selected for analysis. The four white matter structures chosen were the minor forceps, the posterior internal capsules, and the genu and the splenium of the corpus callosum. The structures selected for analysis in the gray matter were the head of the caudate nucleus, the cingulate gyrus, the putamen and the thalamus. These structures were chosen based upon previous results that indicated variations between them in geometric mean T_2, individual peak and distribution widths, and myelin water fraction [16]. An axial image illustrating the 8 regions of interest (ROI) is shown

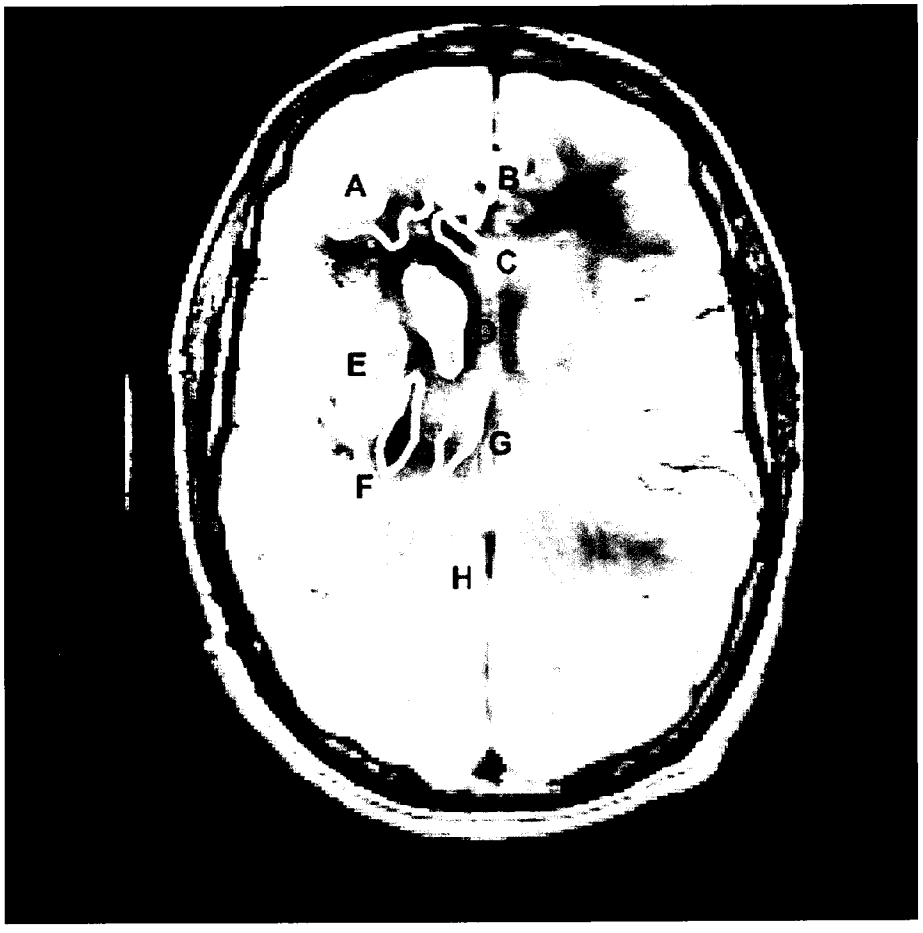

Figure 3.1: The 8 structures that were examined in the brains of human volunteers. Note that this image shows only those occurring on the right side of the brain, however the complete analysis was conducted on both sides of the brain for each structure. The structures are A) Minor forceps; B)Cingulate gyrus; C) Genu of corpus callosum; D) Head of caudate nucleus; E) Putamen; F) Posterior internal capsules; G) Thalamus; H) Splenium of corpus callosum.

in figure 3.1 for the right side of the brain from a normal volunteer. Due to symmetry in the brain, ROIs around each structure were drawn and analyzed from both the left and right sides of the brain. Therefore, a total of 16 ROIs were drawn on each transverse slice from each volunteer.

3.2.3 MRI Pulse Sequence and Imaging Parameters

The pulse sequence used for this study was unique because it permitted two different echo spacings to be used within the same TR. This is a significant difference from other sequences with a constant TE because it allows both short and long echo spacings to be combined. This combination of different echo

spacings leads to better sampling of the decay curves resulting from short relaxing and long relaxing water environments within the brain. Sectioning the pulse sequence allows the last echo to be acquired at long times without sacrificing relaxation information immediately following the 90° excitation pulse.

All volunteers were scanned using a standard quadrature birdcage head coil on a 1.5 T General Electric Horizon Signa scanner with EchoSpeed gradients. A 48-echo CPMG spin-echo pulse sequence with two echo spacings per TR was used. All other imaging parameters except the echo spacing of the final 16 echoes of the 48-echo sequence were unchanged throughout this study. These parameters are shown in table 3.1. A pulse sequence timing diagram of a 32-echo pulse sequence similar to that used in this study is shown in figure 3.2.

Parameter	*Setting*	*Parameter*	*Setting*
Repetition Time (TR)	3 800 ms	TE (echoes 1 – 32)	10 ms
Field-of-view (FOV)	24 x 24 cm	Slice Thickness	5 mm
Acquisition Matrix	256 x 128	Number of Excitations (NEX)	2
Acquisition Time	16:21	Bandwidth (BW)	31.2 kHz

Table 3.1: Imaging parameters used for scanning of human volunteers.

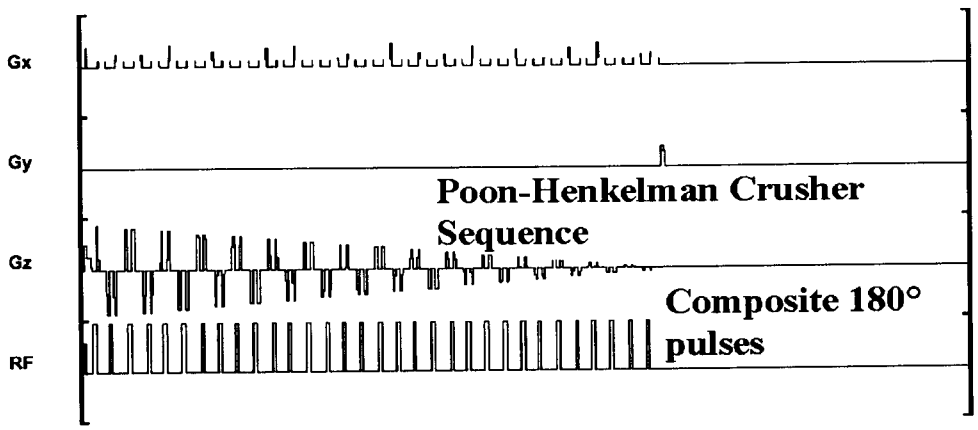

Figure 3.2: A 32-echo CPMG pulse sequence similar to the 48-echo sequence used in this thesis. The Poon-Henkelman crusher sequence is composed of 2 crushers surrounding each 180° refocussing pulse. The amplitude of the crushers are altered to eliminate propagation of unwanted signal from stimulated echoes. The 180° pulses were composite (90_X-180_Y-90_X) in order to provide a more uniform 180° rotation across the slices.

Figure 3.2 illustrates an abbreviated version of the pulse sequence used. The sequence of figure 3.2 contains only 32 refocussing pulses instead of the 48 employed in this study, however the underlying characteristics were the same. The RF pulses used for refocussing were composite pulses that used a sequence of $90^{\circ}_{X} - 180^{\circ}_{Y} - 90^{\circ}_{X}$ rather than 180°_{Y}. The 180° pulses were applied between two 90° pulses to eliminate imperfections caused by a non-uniform RF field across the selected slice. Before and after the 180° pulse was applied, the slice select gradient was turned on and used the Poon-Henkelman crusher sequence. The crushers eliminate any signal originating from outside the slice of interest as well as prevent unwanted signal due to stimulated echoes.

This study examined 5 variants of a 48-echo pulse sequence. These sequences differed from one another by employing different echo spacings later in the pulse sequence. To preserve information about the short-T_2 and intermediate-T_2 components, due to myelin water and intracellular/extracellular water respectively, the first 32 180° refocussing pulses had an echo spacing of 10 ms in each of the 5 combinations. This echo spacing will be referred to as the *primary echo spacing*. The primary echo spacing was held at 10 ms because previous studies showed the myelin and intra/extracellular water compartments to have T_2 relaxation times of 0 – 50 ms and 70 – 90 ms respectively. Therefore to properly sample the early sections of the decay curves, the minimum echo spacing was preferred. A small echo spacing permits closely spaced data to be acquired in this early time regime. The final 16 180° refocussing pulses, the *secondary echo spacing*, varied in each of the 5 sequences tested. The 5 secondary echo spacings used were 10, 20, 30, 40, and 50 ms and resulted in the last echo being of each sequence acquired at 480, 640, 800, 960 or 1120 ms respectively. The first sequence used a secondary echo spacing of 10 ms, which made it equivalent to a 48-echo sequence with a single TE. The volunteers were scanned 5 times each through the same transverse plane and a different secondary echo spacing was selected for each scan.

Following data acquisition on the MR scanner, the 48-echo data sets were converted into a format suitable for viewing. For each volunteer, regions of

interest (ROI) were drawn on the axial slice acquired for each of the 5 different echo spacings tested. ROIs around each of the eight brain structures of figure 3.1 were drawn, on both the left and right side of the brain, for a total of 16 ROIs per secondary echo spacing per volunteer. A total of 800 ROIs were examined for the set of 10 volunteers.

The ROIs from each volunteer each volunteer were processed in order to generate the T_2 decay curves for each structure, on both sides of the brain. These decay curves were input into a least-squares fitting algorithm, (section 3.3) and solutions were found to describe their relaxation properties.

3.3 Phantoms

The goal of this thesis was to optimize a 48-echo pulse sequence to allow better *in-vivo* determination of the various T_2 components from patients afflicted with MS. In the absence of patients with MS available for study, it was necessary to simulate the effect of the different pulse sequences on phantoms whose T_2 relaxation characteristics were similar to those of the cerebral tissue of MS patients. To this end a set of nickel chloride ($NiCl_2$) doped agarose phantoms that had T_1 and T_2 relaxation times similar to cerebral tissue were imaged.

3.3.1 Phantom Composition

A total of 8 water phantoms were studied, each of which had been previously created according to the recipe of Mitchell *et al* [44]. $NiCl_2$ was used as the doping agent because its T_2 relaxation has been shown to have a relative independence to both temperature and field strength [45, 46]. The phantoms were contained within vacuum-sealed glass tubes, which minimized water evaporation during storage. The glass tubes had a diameter of 1 cm and a length of 16 cm. From shortest to longest, the T_2 relaxation times of the 8 phantoms scanned were: 24, 29, 80, 97, 110, 178, 286, and 444 ms.

3.3.2 MRI Pulse Sequence and Imaging Parameters

The $NiCl_2$ phantoms were imaged using the same pulse sequence as that used for the normal volunteers, described above in section 3.1.2. A 48-echo CPMG pulse sequence with two different echo spacings, a primary echo spacing of 10 ms and a secondary echo spacing that ranged from 10 ms to 50 ms, in 10 ms intervals, was employed. The other imaging parameters were the same as those in table 3.1 except the FOV was reduced to 24 x 12 cm. The half-FOV reduced the acquisition time by a factor of 2 to 8:06 but did not affect the size of the acquisition matrix. To accurately determine the T_2 characteristics of the phantoms, an additional 2 pulse sequences were included in the protocol. Both were 48-echo CPMG sequences but these sequences used constant echo spacings throughout each TR. These echo spacings were chosen to be 20 ms and 30 ms with the final echoes from each sequence acquired at 960 ms and 1440 ms respectively.

Each phantom was scanned individually while placed at the center of a head phantom loader shell (#46-28790063, General Electric) that contained distilled water. The loader shell had an inner diameter of 20.6 cm, an outer diameter of 23.3 cm, and a length of 18 cm. The phantoms were tipped at a small angle of approximately 5° to prevent bubbles from accumulating along the upper edge of the tube during imaging. One transverse slice was acquired through the center of each phantom.

3.3.3 Phantom Simulation of Multiple Sclerosis Lesions

To mimic the relaxation characteristics of MS lesions, the 8 individual phantoms were combined in different proportions. The phantoms were known to each have a monoexponential decay curve, a fact that was confirmed following imaging of the individual tubes. To create a mixture that contained T_2 relaxation characteristics similar to that of MS lesions, these individual decay curves were combined in specific proportions. MS lesions are associated with regions of demyelinated axons. We assume that in regions where lesions are present there water will exist in a state that permits greater mobility than intra/extracellular

water. Because the water associated with lesions does not have as great a mobility as free water or water within CSF, the T_2 time of lesion water compartment is expected to occur between the 70 – 90 ms and 1 s T_2 relaxation times of compartmentalized intra/extracellular water and CSF respectively. We hypothesize that the water compartment associated with MS lesions possess a T_2 relaxation time in the range of 200 – 500 ms.

Following imaging, the 8 phantoms, specifically their decay curves, were divided into 3 groups representing the three principle water compartments (excluding CSF) present in the brain of MS patients. The first group, the myelin water compartment, used the phantoms with T_2 relaxation times of 24 and 29 ms. The second group, representing intra/extracellular water, contained the phantoms whose T_2 time constants were 80 ms, 97 ms and 110 ms. The third group contained the 178 ms, 286 ms, and 444 ms phantoms, and represents the peak unique to MS lesions.

Before combining the monoexponential decay curves, they were normalized to the t = 0 amplitude. Normalization was performed because each tube had been imaged separately and thus the peak amplitudes varied. A normalized decay curve from each of the three groups was combined with a decay curve from each of the other two groups. Such combinations produced normalized triexponential decay curves. The fractional contribution of each monoexponential decay curve to the triexponential curve was based upon previously measured values of each within the brain [16]. Three different fractional contributions for each component were used in this study. The percentage contributions used were 10:80:10, 15:70:15 and 15:75:10. In these ratios, the first percentage is that contributed by myelin water, the second by intra/extracellular water and the third by the water associated with a lesion. All possible combinations of the members of the three groups of phantoms were completed for a total of 18 triexponential data sets.

3.4 Non-Negative Least Squares Relaxation Analysis

The analysis of NMR relaxation of inhomogeneous systems often requires that the decay curves be approximated as the sum of multiple exponential components. If a system has only a single component and it decays with a monoexponential character, or if the system has two components with very different time constants, then a very accurate estimate of T_2 is possible. In systems, such as the human brain, which demonstrate multiexponential relaxation it is necessary to employ a non-trivial estimation method for the determination of T_2. For the 48-echo decay curves acquired from the both volunteers and $NiCl_2$ agarose phantoms, a least squares fitting algorithm was applied to determine the T_2 relaxation components. Specifically, the two data sets were analyzed using a non-negative least squares (NNLS) fitting routine [24]. The NNLS algorithm allowed the determination of the T_2 distribution of both the individual cerebral structures and the water based phantoms. Based upon these results, calculations were made of the geometric mean T_2, which is the mean of the distribution on a logarithmic scale, the width of individual peaks in the distribution, and the myelin water fractions in different structures. As this algorithm was the foundation of the results to be presented in the next two chapters, a brief overview of relaxation analysis and the NNLS algorithm will now be introduced.

The NNLS algorithm decomposes decay curves into an arbitrary number of exponential terms, however it is not a requirement of the system to have multiexponential character. Application of NNLS to a monoexponential system will produce a solution with a single T_2 relaxation time. In general multiexponential systems can be described by the following integral equation

$$y(t_i) = y_i = \int_{T_{min}}^{T_{max}} s(T)\exp\{-t_i/T\}dT \qquad i = 1, 2,\ldots, N \qquad (3.1)$$

In equation 3.1 the N data y_i are measured at times t_i and $s(T)$ is the unknown amplitude of the component whose relaxation time is T [24]. Equation 3.1 represents a continuous distribution of relaxation times. If it is assumed that the

true T_2 distribution is a sum of M delta functions and each has an area of s_j then equation 3.1 can be rewritten as a discrete sum of exponential terms or

$$y_i = \sum_{j=1}^{M} s_j \exp\{-t_i / T_j\} \qquad i = 1, 2, \ldots, \ N \qquad (3.2)$$

Equation 3.2 assumes that the spectrum is a sum of M delta functions, the number of which is set to be great enough such that the solution is not biased towards a small number of exponentials. M is normally on the order of 100 or 200 terms. In the analysis of the decay curves from the 48-echo pulse sequence presented in the following chapters, the data was decomposed into a set of 120 exponential terms spaced logarithmically from 15 ms to 2 s.

In magnetic resonance imaging, the measured data are contaminated by noise and therefore equation 3.2 should not be solved exactly. Instead the data must be misfit by an amount that is consistent with the uncertainty present in the measured data. The degree of misfit in between the measured data, y_i, and the predicted data, y_i^p is given by χ^2, defined by

$$\chi^2 = \sum_{i=1}^{N} (y_i^p - y_i)^2 / \sigma_i^2 \qquad (3.3)$$

In equation 3.3, σ_i is the standard deviation of the ith datum. In the 48-echo pulse sequence used in this thesis, the decay curve is sampled at 48 points in time, thus N = 48. The preferred solution should fit these data such that $\chi^2 \approx N$ so that each datum is fit to within one standard deviation. If $\chi^2 << N$ then the data are fit too accurately and extra components in the distribution may be present as a result of noise in the measured data. Conversely, if $\chi^2 >> N$ the data are not fit well enough and information about the system may be lost.

Two methods of least-squares analysis were used to determine the T_2 distributions of the measured data, regularized and non-regularized NNLS. With non-regularized NNLS the least-squares fitting was performed simply through minimization of χ^2. For a multiexponential system, non-regularized NNLS yields a solution composed of delta functions at a few isolated relaxation times. Unfortunately, this solution is sensitive to noisy data and can cause delta

functions that are not true time constants of the system to appear in the T_2 distribution. The regularized NNLS routine minimizes χ^2 but it also minimizes the roughness of the solution. Regularized NNLS contains an additional term, known as a regularizer, which balances minimization of the misfit with smoothness in the resulting T_2 distribution. Minimization of both χ^2 and solution roughness leads to a smooth distribution with a small number of exponential terms. Figure 3.3A shows a typical non-regularized T_2 distribution while in figure 3.3B both the χ^2 misfit and the solution roughness have been minimized to produce a much smoother spectrum. The true T_2 distribution in brain is likely composed of a continuous distribution of relaxation times and as such the distribution shown in figure 3.3b may be better for analyzing relaxation in cerebral tissue. Regularized

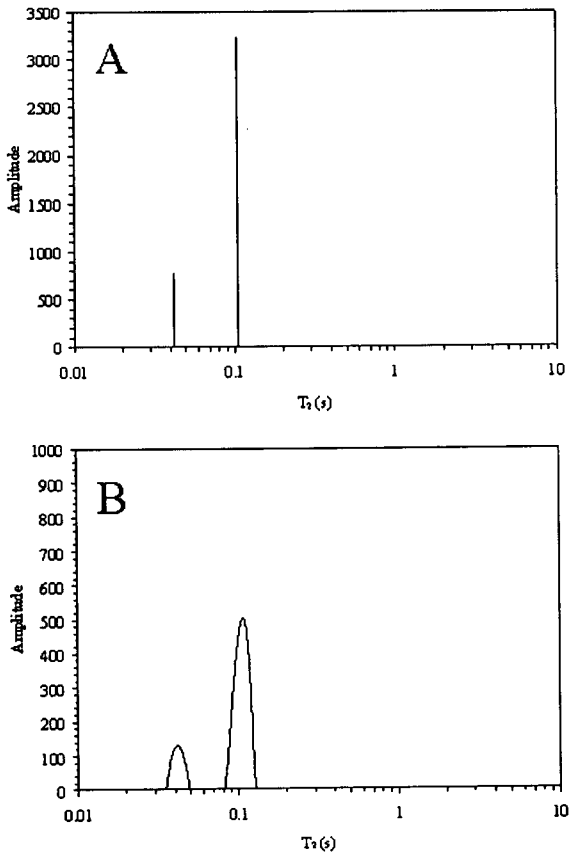

Figure 3.3: T_2 distributions generated using A) non-regularized NNLS where the misfit, χ^2, is minimized and B) regularized NNLS where both χ^2 and the solution roughness are minimized. The sum of the amplitudes of each distribution are equivalent.

NNLS is more robust in the presence of noise and is thus not as susceptible to generating spurious spikes that are not representative of the relaxation properties of the system.

Both the non-regularized and the regularized NNLS algorithms were performed using 120 relaxation times separated logarithmically over the range of 15 ms to 2 s. The algorithm terminated when χ^2 fell between 1.02 and 1.025 times the minimum χ^2 from non-regularized method. Therefore the χ^2 was allowed to increase to between 2 % and 2.5 % of its minimum value.

The NNLS solutions were subsequently used by a previously written statistics package to calculate the geometric mean T_2 (GM T_2), the myelin water fraction (MWF), and the width of the individual peaks of the distributions. For the *in-vivo* study, GM T_2 was calculated for the myelin water and the intra/extracellular water compartments. The range of T_2 chosen for calculation of myelin's GM T_2 was 0 – 50 ms. The intra/extracellular water GM T_2 calculation used a range of 50 – 400 ms. These two ranges correspond to the principle non-CSF compartments determined from the literature [16]. The range selected for the determination of GM T_2 for the phantom study was based upon the location of the peaks in the distribution. The myelin water fractions, MWF, were calculated by dividing the signal intensity from 0 – 50 ms in the T_2 distribution by the signal intensity between 0 – 700 ms (excluding CSF) *in-vivo*, and by the signal from the entire distribution in the phantom study. The ranges differed because the ROIs drawn on the *in-vivo* images may have contained small amounts of CSF and this component had to be eliminated when calculating the MWF. However, this was not a problem when phantoms were imaged because the components of the decay curves were known prior to the analysis. To describe the dependency that the width of individual peaks had on the secondary echo spacing, the width for specific regions was also calculated.

Chapter 4: In-vivo Results

4.1 Introduction

A 48-echo CPMG pulse sequence was used for imaging a series of 10 healthy volunteers. The pulse sequence allowed two echo spacings to be used. The primary echo spacing (PES) contained the first 32 echoes and secondary echo spacing (SES) contained the final 16 echoes. The PES was 10 ms for all experiments, while the SES was cycled through 5 different values, which were 10, 20, 30, 40 and 50 ms. The 48-echo sequence where the PES and SES were 10 ms was equivalent to a constant echo spacing sequence.

The normal volunteers were selected to test whether pulse sequences with extended SESs (greater than 10 ms) were more effective in extracting valuable T_2 relaxation information about the various water compartments within the brain. Based on T_2 distributions generated by NNLS, other parameters such as the geometric mean T_2 for a given region of the distribution, the myelin water fraction, and the width of individual peaks were calculated.

The goal of the *in-vivo* imaging experiments was two-fold. First, we aimed to determine how the multiple echo spacing sequences performed compared to the constant TE sequence. Second, it was also desirable to find which of the 5 pulse sequences was optimal in extracting the T_2 information from the decay curves. This chapter will show the results of this study. Sample T_2 distributions are first presented from each of the 8 regions of interest in the brain. For each of the sequences, calculations of the geometric mean T_2, the width of the main water peak and the myelin water fractions in the white matter structures are presented. Finally, the main findings of the *in-vivo* study are discussed.

4.2 Results

4.2.1 T_2 Distributions

The regions of interest in the images from the 10 volunteers imaged were outlined and processed to yield decay curves of the measured signal at each echo. Figure 4.1 shows two such decay curves from one gray matter structure,

the head of the caudate nucleus, and one white matter structure, the posterior internal capsules. The curves of 4.1a and 4.1b are from a sequence with a SES of 50 ms. The solid lines on each curve are the regularized NNLS solutions to their respective data sets.

The decay curves from each ROI were input into the NNLS algorithm to generate T_2 distributions. Figures 4.1a and 4.1b show the regularized NNLS solution superimposed upon the measured data. For each of the 5 pulse sequences, 16 ROIs (8 structures per side of the brain) were drawn for each volunteer. Because the human brain likely contains a continuum of T_2 times the regularized NNLS solutions were chosen for analysis of the in-vivo data and are presented in this chapter. These are used because the regularized solutions are calculated through minimization of the misfit, χ^2, and solution roughness whereas the non-regularized solution minimized only the χ^2 statistic.

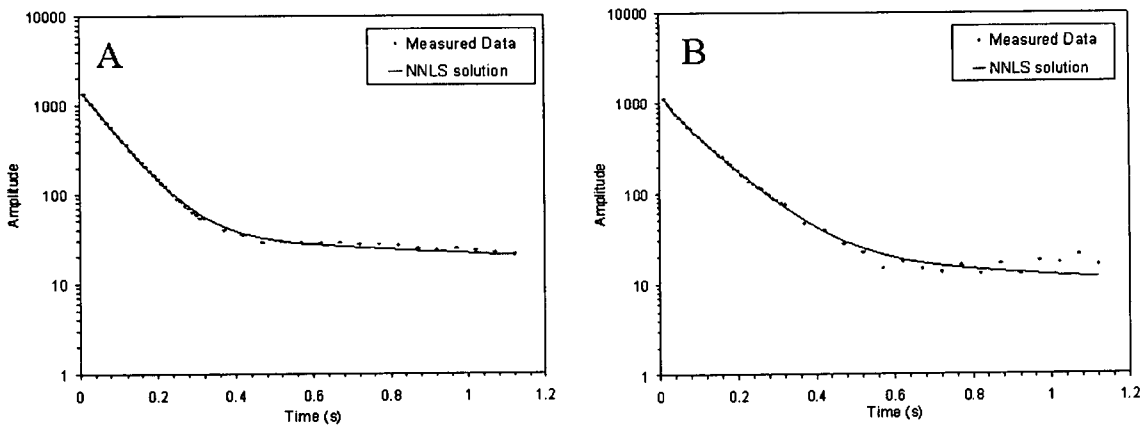

Figure 4.1: Decay curves showing measured data (♦) and the standard error from A) head of the caudate nucleus and B) the posterior internal capsules. The solid line is the regularized NNLS solution to the data.

The T_2 distributions that were calculated using regularized NNLS for the 4 gray matter structures examined are shown in figures 4.2, 4.3, 4.4 and 4.5. Each figure contains 4 out of the 20 T_2 distributions that were produced from each structure from the 10 volunteers. The 4 gray matter structures were the head of the caudate nucleus, the cingulate gyrus, the putamen and the thalamus.

For the 5 SESs tested, the T_2 distributions consistently yielded a single, strong main peak whose T_2 location varied from a low T_2 of 74 ms (putamen) to a high of 94 ms (cingulate gyrus). This variation in the geometric mean T_2 is consistent with previous studies [16]. The results within the gray matter do not indicate which pulse sequence of the 5 tested is optimal as each yielded its main water peak at T_2 times that were within experimental error of each other.

The T_2 distributions for the four structures of the gray matter indicated that a single, relaxing component was dominant. The single component implied that the lifetime of water in the different gray matter regions was similar and that only a minimal barrier to the motion of water molecules was present. The single peak on the distribution in the different structures also demonstrated that the water environments were homogeneous within different structures. Also, the width of the main peak in gray matter regions are relative and not absolute and are consequence of regularized NNLS minimizing solution roughness.

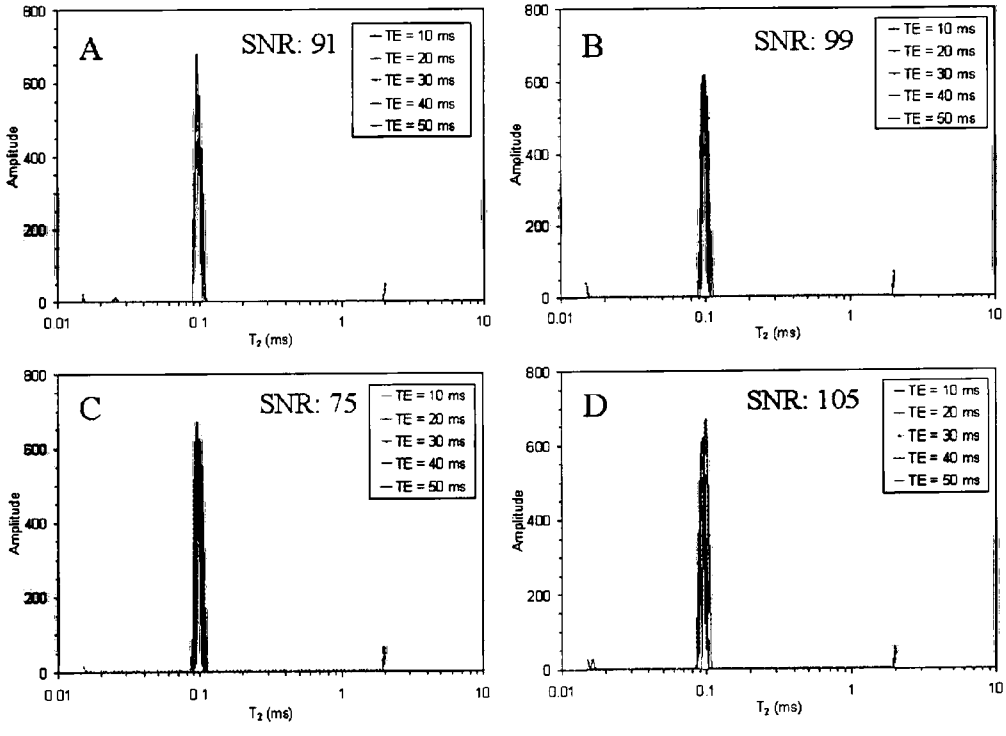

Figure 4.2: Cingulate gyrus (CG) regularized NNLS T_2 distribution from 4 volunteers. The mean per pixel SNR from the CG was 87.2 ± 26.8. The TE times listed in the legend are the secondary echo spacings for each pulse sequence evaluated. For all sequences the primary echo spacing was 10 ms.

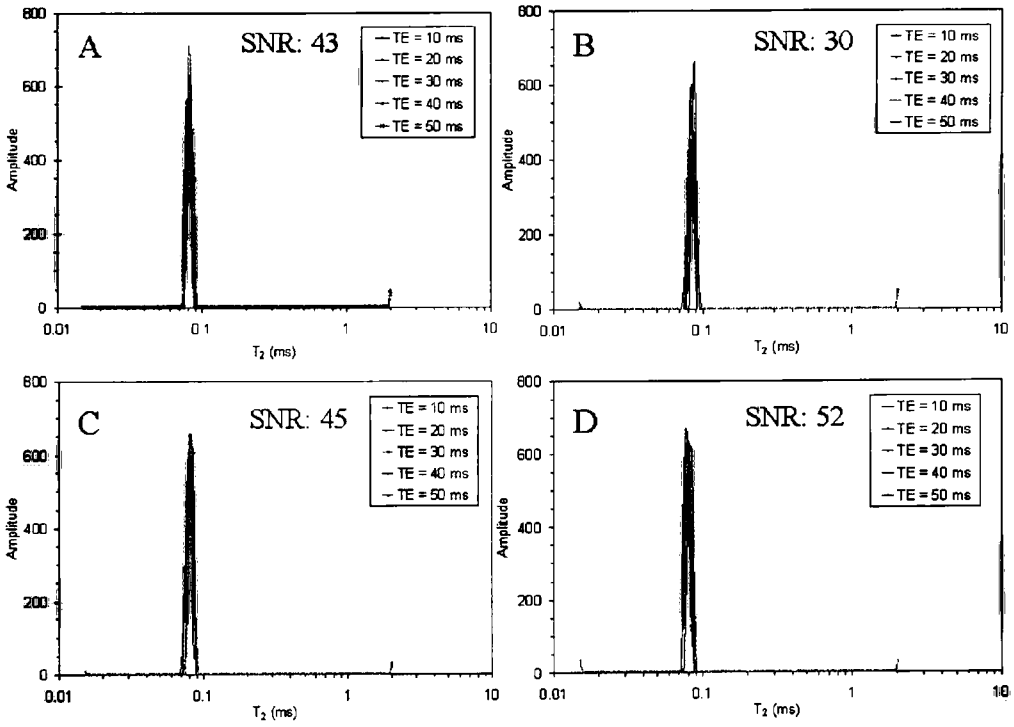

Figure 4.3: Head of the caudate nucleus (CH) regularized NNLS T_2 distributions from 4 volunteers. The mean per pixel SNR from the CH was 40.5 ± 19.3.

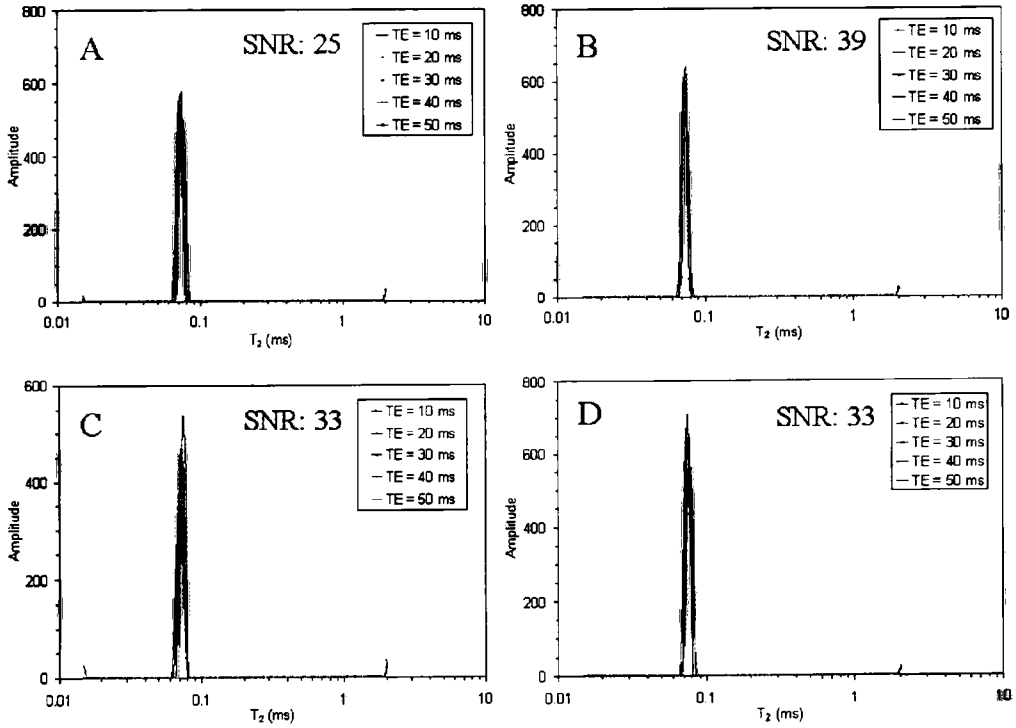

Figure 4.4: Putamen (P) regularized NNLS T_2 distributions from 4 volunteers for the 5 pulse sequences that were evaluated. The mean per pixel SNR was 38.3 ± 18.8 in the putamen.

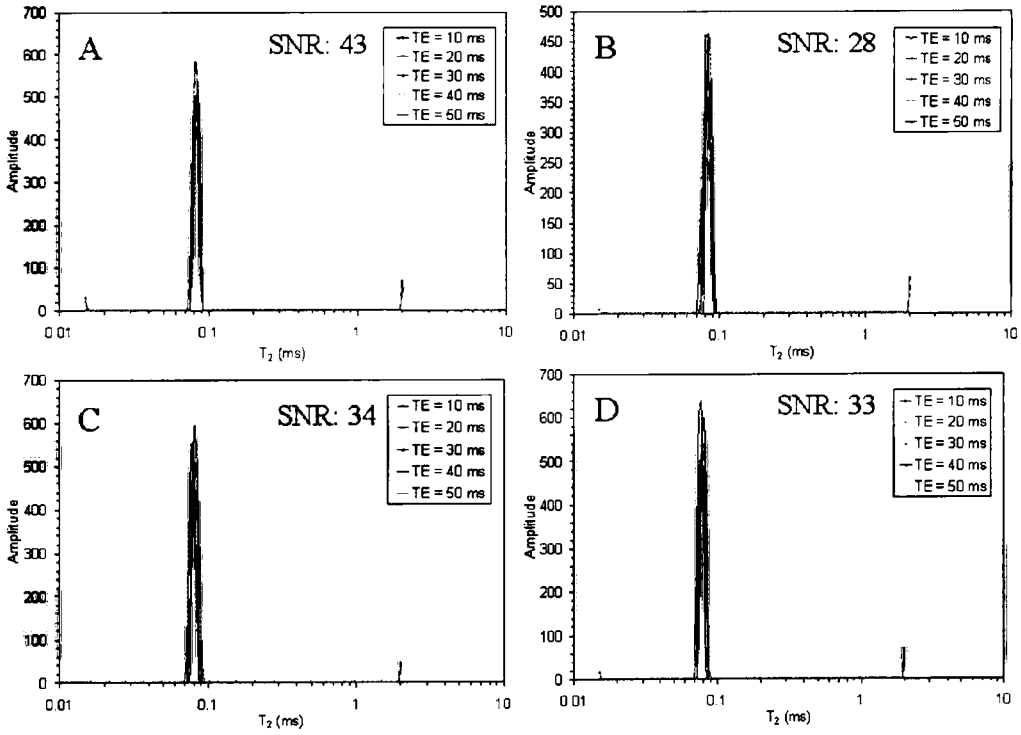

Figure 4.5: Thalamus (T) regularized NNLS T_2 distributions from 4 volunteers for the 5 pulse sequences that were evaluated. The mean per pixel SNR in the thalamus was 40.3 ± 17.4.

Four white matter regions were also chosen to test the 5 pulse sequences and T_2 distributions were subsequently generated. These 4 structures were the genu of the corpus callosum, the minor forceps, the posterior internal capsules and the splenium of the corpus callosum. A sample of 4 distributions from the 20 produced are shown below in figures 4.6 – 4.9.

The T_2 distributions in the white matter demonstrate that the modified 48-echo pulse sequence with an extended SES (40 and 50 ms) leads to an increase in resolution of both the myelin water peak and the main intra/extracellular water peak. In many of the T_2 distributions from white matter, for the sequences that used a short SES of 10 and 20 ms, distinguishing the short T_2 component was difficult.

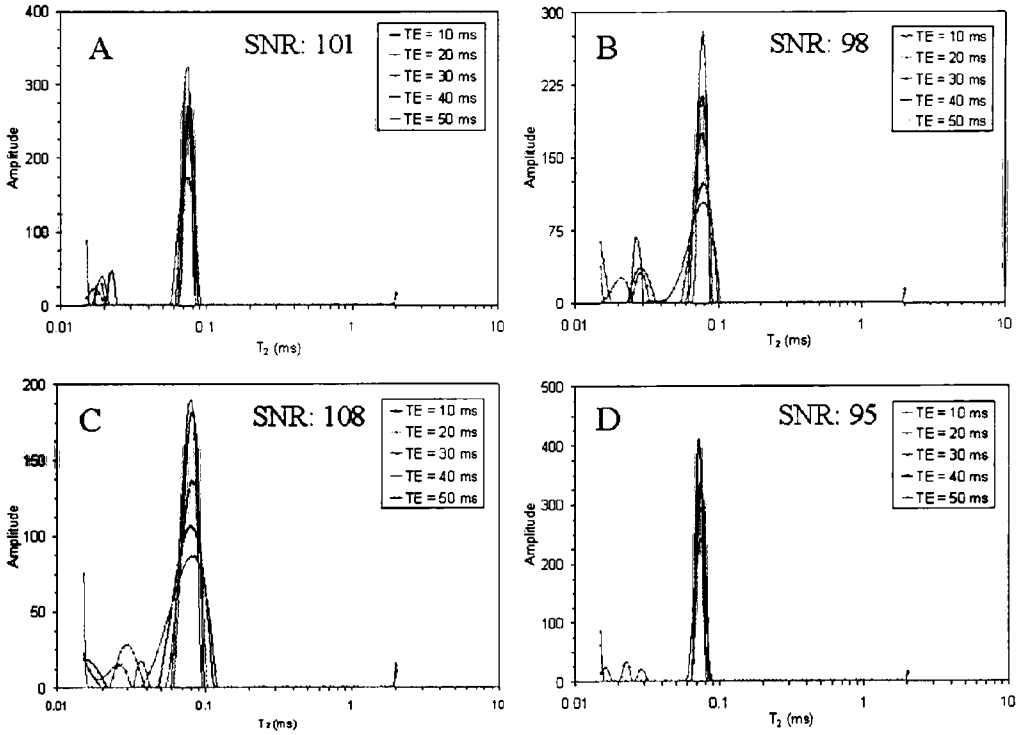

Figure 4.6: Genu of corpus callosum (GCC) regularized NNLS T_2 distributions from 4 volunteers for the 5 pulse sequences evaluated. The mean per pixel SNR in the GCC was 88.7 ± 28.9.

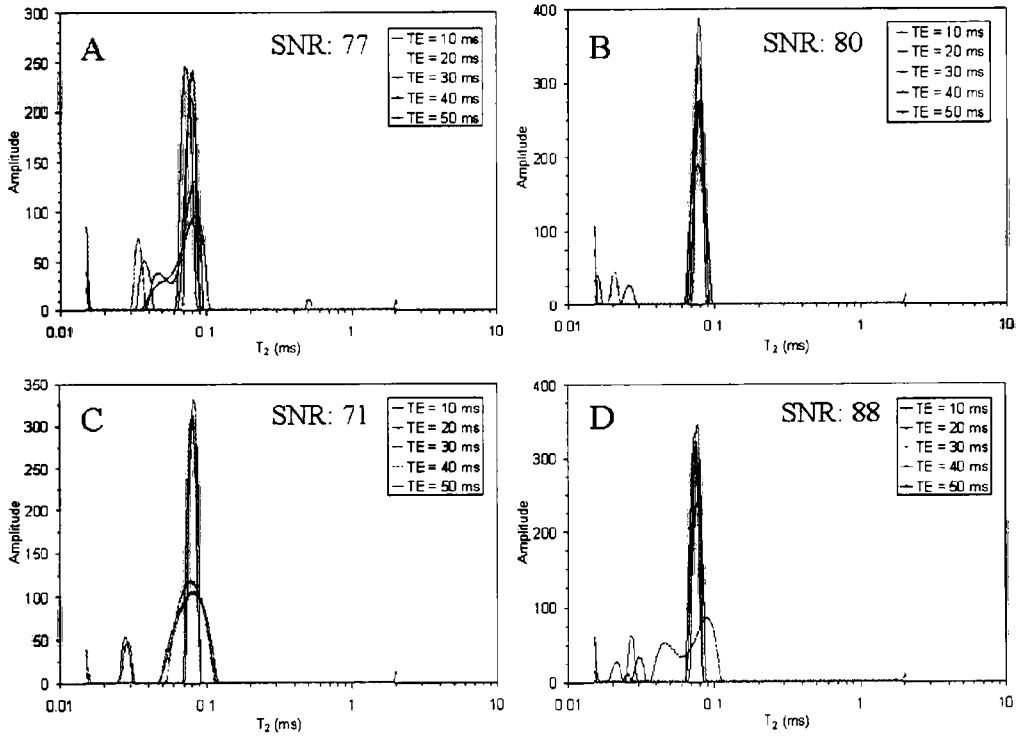

Figure 4.7: Minor forceps (MF) regularized NNLS T_2 distributions from 4 volunteers. The mean per pixel SNR in the MF was 75.0 ± 19.2.

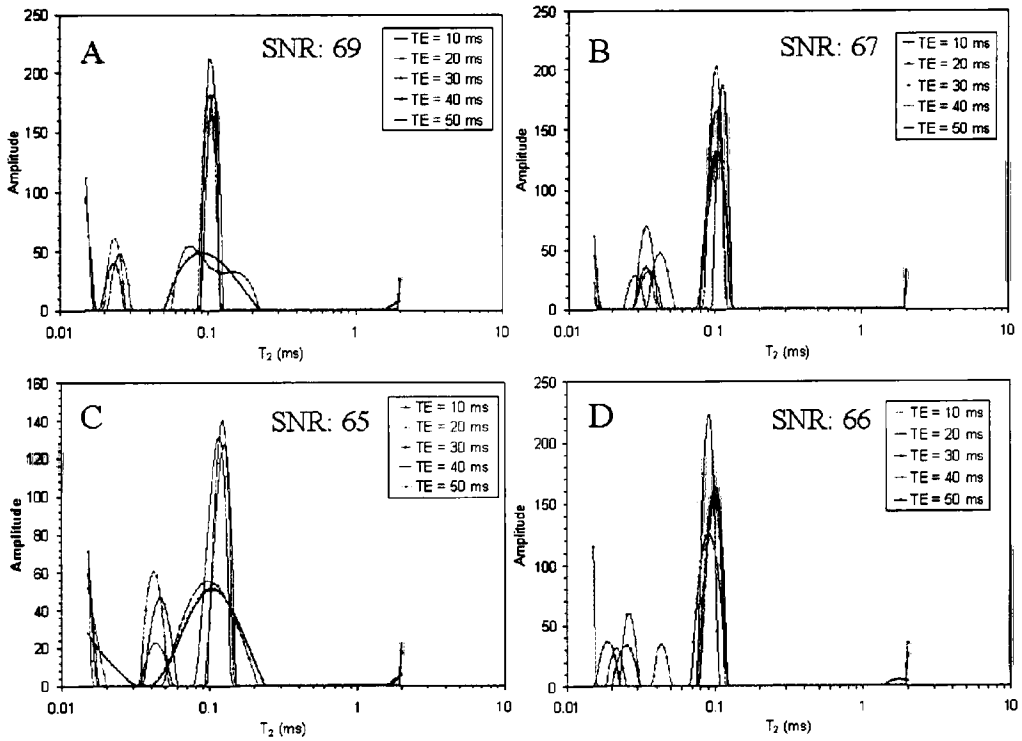

Figure 4.8: Posterior internal capsules (PIC) regularized NNLS T_2 distributions from 4 volunteers. The mean per pixel SNR in the PIC was 64.1 ± 17.6.

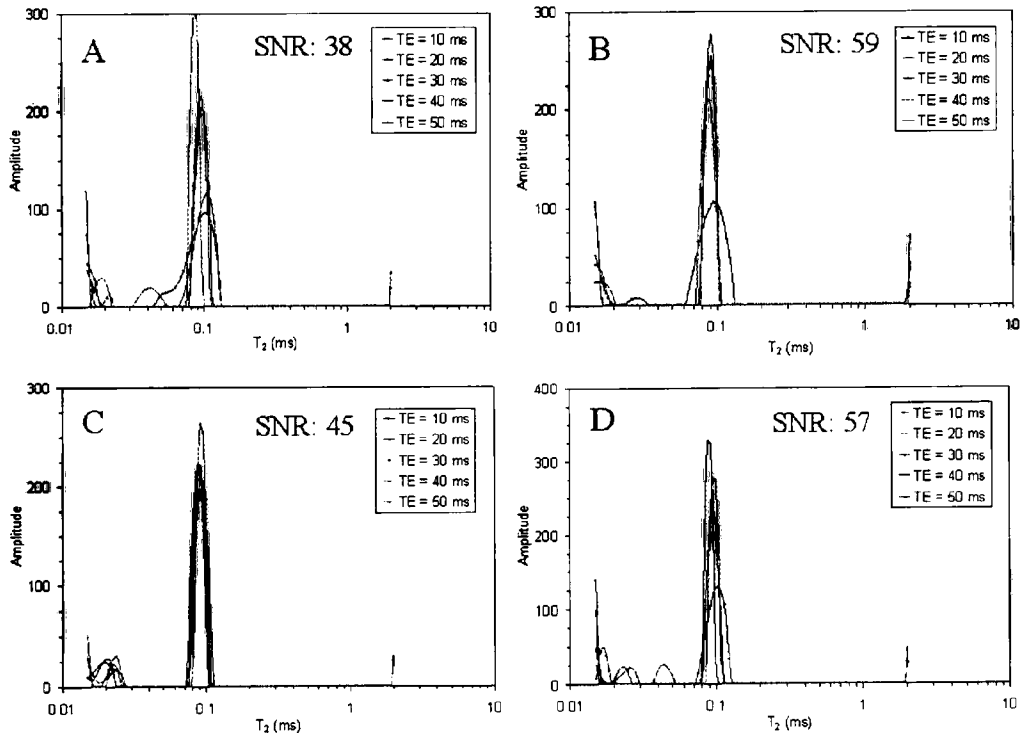

Figure 4.9: Splenium of corpus callosum (SCC) regularized NNLS T_2 distributions from 4 volunteers. The mean per pixel SNR in the SCC was 51.5 ± 20.5.

4.2.2 Signal-to-Noise Considerations

The signal-to-noise ratio (SNR) for each distribution and the mean SNR for each structure over 20 volunteers is given in figures 4.2 – 4.9. The SNR was fluctuated between different structures, particularly between the white and gray matter regions. Furthermore, while the SNR from structure to structure varied, between different volunteers only minor fluctuations occurred. The highest SNR occurred in the cingulate gyrus while the lowest was seen in the putamen although the caudate nucleus and the thalamus were very similar to the putamen. This indicated that the SNR of the cingulate gyrus may have been increased artificially by surrounding regions, specifically cerebrospinal fluid (CSF).

The cingulate gyrus is a convoluted, frontal lobe structure whose edges border the midline of the brain and is adjacent to regions that contain CSF. Due to the difficulty encountered in drawing ROIs around the cingulate gyrus, it is possible that the ROIs included a number of pixels outside its boundary that contained the slowly relaxing CSF. If CSF was present in the ROI then there would have been more signal present during late echoes. The SNR was calculated by dividing the t = 0 amplitude by the standard deviation of the residuals of the fit. If greater signal was present at the latter echoes then the NNLS solution would have fit the data better because it would be less contaminated by noise. In this situation the residuals would be smaller as would their standard deviation.

In white matter structures it was found that the SNR was consistently higher than the SNR within the gray matter regions (except in the cingulate gyrus). The white matter region with the greatest SNR was the genu of the corpus callosum and the area with the lowest SNR was found to be the splenium of the corpus callosum.

The SNR also decreased as a function of the SES. An example of this is shown in figure 4.10 in both white and gray matter. To determine the per pixel SNR shown in figure 4.10 the SNR of the entire ROI was first calculated. Over the entire ROI the SNR is found by dividing the t = 0 amplitude of the decay

curve by the residuals from the NNLS fit. The per pixel SNR is then found by dividing the SNR of the ROI by the square root of the number of pixels within the ROI. The decrease in SNR shown in both gray and white was expected because of the NNLS algorithm. As SES was increased, the decay curve was sampled

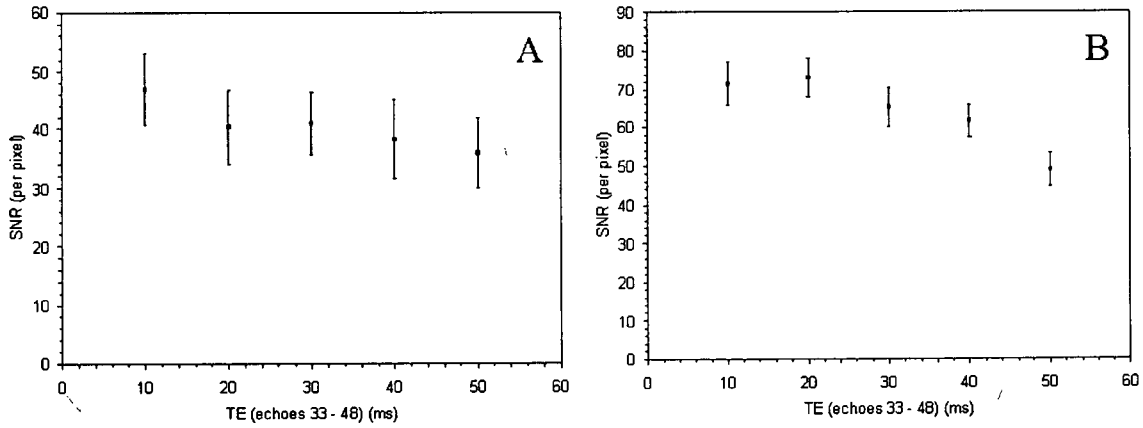

Figure 4.10: The mean SNR per pixel decreased as the secondary echo spacing increased for gray and white matter structures. The per pixel SNR for the A) head of the caudate nucleus and B) the posterior internal capsules is shown.

at progressively longer times and at these times the signal became closer to the noise, which is equivalent to a baseline offset. The NNLS algorithm calculated the T_2 distributions by fitting the entire decay curve, and as a result the fit is poorer in the later time because the measured data are more affected by noise than those points at early times.

4.2.3 Geometric Mean T_2

Following application of NNLS to yield T_2 distributions for each structure, several parameters were calculated to quantify peak locations and their properties in each T_2 spectrum. The first parameter used to describe the location of the individual peaks is the geometric mean T_2 (GM T_2), which is the mean of the distribution, or portion of the distribution, measured using a logarithmic scale. In tables 4.1 and 4.2 the mean (N = 20) GM T_2 values of the main intra/extracellular water peak are shown for the 4 gray matter and the 4 white matter structures respectively. For each structure the corresponding GM T_2 is

Structure	TE (ms)	Mean GM T_2 (ms)	GM T_2 (ms) [16]
Head of caudate nucleus	10	81.6 (1.0)	79.5 (1.0)
	20	80.7 (0.6)	
	30	81.3 (0.7)	
	40	80.4 (0.7)	
	50	79.9 (0.8)	
Cingulate Gyrus	10	94.0 (0.8)	85.5 (1.3)
	30	94.0 (0.9)	
	30	94.0 (0.8)	
	40	93.0 (0.9)	
	50	92.7 (1.0)	
Putamen	10	74.2 (0.8)	73.9 (0.7)
	30	73.4 (0.5)	
	30	73.5 (0.6)	
	40	74.0 (0.5)	
	50	73.1 (0.6)	
Thalamus	10	81.5 (0.9)	76.3 (0.7)
	30	80.4 (1.0)	
	30	80.2 (0.7)	
	40	79.3 (0.7)	
	50	79.4 (0.7)	

Table 4.1: Mean GM T_2 (standard error) of the main water peak in 4 gray matter structures for 5 pulse sequences. The data are compared to previous results [16].

Structure	TE (ms)	Mean GM T_2 (ms)	GM T_2 (ms) [16]
Genu of Corpus Callosum	10	72.9 (0.8)	71.1 (0.9)
	20	72.9 (0.5)	
	30	73.2 (0.6)	
	40	73.7 (0.6)	
	50	73.0 (0.7)	
Minor Forceps	10	75.8 (0.6)	70.3 (1.2)
	30	76.0 (0.6)	
	30	76.5 (0.6)	
	40	76.4 (0.8)	
	50	76.0 (0.7)	
Posterior Internal Capsules	10	94.3 (1.3)	82.5 (1.2)
	30	96.4 (1.4)	
	30	95.8 (1.4)	
	40	97.6 (2.0)	
	50	95.5 (1.4)	
Splenium of Corpus Callosum	10	88.4 (1.4)	82.0 (1.1)
	30	91.0 (1.7)	
	30	89.2 (1.6)	
	40	89.6 (1.4)	
	50	89.4 (1.6)	

Table 4.2: Mean GM T_2 (standard error) of the main water peak in 4 white matter structures for 5 pulse sequences. The data are compared to previous results [16].

presented from a previous study [16]. The range used to find the GM T_2 for the mainpeak was 50 – 400 ms for all structures. As can be seen from the table 4.1 and 4.2, the calculated GM T_2 was very accurate in the gray matter when compared to the previous results, except in the case of the cingulate gyrus. The reason for the higher GM T_2 in the cingulate gyrus was the difficulty in drawing the ROI around the edges of the structure without including regions containing CSF. CSF within the ROI may have caused a longer estimate of the T_2 time for the cingulate gyrus. In white matter the calculated values did not agree as well with the study of Whittall *et al.* A cause of this is that Whittall *et al.* used a 32-echo pulse sequence (TE = 10 ms; TR = 3 s) and a range of 50 – 150 ms to span the main peak in their distributions. The range in this study was extended to 400 ms to completely span the main peaks because in some of T_2 distributions the width of the main peak was greater than 150 ms. Therefore, any T_2 components that were part of the main peak above 150 ms were included in the GM T_2 calculation. Also, sampling of the main peak in the sequences used here was more complete than that of Whittall *et al.* where the final echo was acquired at 320 ms. In this study, the shortest time that the final echo was sampled was 480 ms for a SES of 10 ms and the longest was 1120 ms when SES was 50 ms. Thus, the NNLS algorithm could more accurately find the true T_2 components in the distribution, especially those around the main intra/extracellular water peak.

The GM T_2 for the myelin water peak was difficult to determine but it was possible to measure the myelin peak areas (MWF) to distinguish differences between the structures of the white matter. The difficulty in measuring these short T_2 times is a result of the fast relaxation of myelin water combined with the relatively long echo spacing (10 ms) early in the pulse sequence. This hindrance was also encountered by Whittall *et al.* where the MWF was determined but the GM T_2 could not be [16]. The white matter T_2 distributions of figures 4.6 – 4.9 demonstrate that using a longer SES is advantageous. As SES was increased through 30, 40 and 50 ms, the NNLS solution an increasingly better defined myelin water peak than with the shorter SES values. This result is again due to better sampling of the decay curve at long times. The increased accuracy in the

fit of the main water peak permits greater information about the short myelin peak to be available for the fitting algorithm. As a result, using longer echo spacings permits both peaks to be better resolved in the resultant T_2 distribution.

4.2.4 Myelin Water Fraction

A second parameter used to describe the short T_2 component in the T_2 distribution is the myelin water fraction (MWF). It was determined based upon the proportion of the total signal that occurred within the region of the distribution attributed to myelin water. From previous work, this window was defined to be between 0 and 50 ms [15, 16].

Structure	TE (ms)	Mean MWF (%)	MWF (%) [16]
Genu of Corpus Callosum	10	7.91 (0.88)	9.86 (0.96)
	20	7.49 (0.75)	
	30	7.66 (1.01)	
	40	8.19 (0.76)	
	50	7.63 (1.07)	
Minor Forceps	10	6.11 (0.97)	8.40 (0.89)
	30	7.14 (0.85)	
	30	7.50 (1.00)	
	40	6.99 (1.09)	
	50	7.35 (1.01)	
Posterior Internal Capsules	10	15.65 (0.94)	15.00 (0.95)
	30	17.64 (1.00)	
	30	19.50 (1.38)	
	40	21.88 (1.62)	
	50	19.52 (1.20)	
Splenium of Corpus Callosum	10	12.22 (1.23)	13.05 (0.96)
	30	15.46 (1.20)	
	30	13.49 (1.27)	
	40	13.57 (0.52)	
	50	13.80 (0.92)	

Table 4.3: The mean myelin water fraction (MWF) (standard error) in 4 white matter structures for the 5 pulse sequences. The data are compared to previous results [16].

The MWF was calculated by dividing the ratio of the signal intensity between 0 and 50 ms by the signal intensity measured between 0 and 700 ms on the T_2 distribution. The upper bound was selected because it was sufficiently high to include T_2 components that may have resulted from the intermediate T_2 component yet significantly lower than the T_2 of CSF. The MWF calculated for

the white matter structures are shown in table 4.3 below. These results were again consistent with the work of Whittall *et al.* This led to the conclusion that splitting the pulse sequence into two sections did not adversely affect measurements of the myelin water component. Conversely, extending the pulse sequence may be beneficial because it permits easier differentiation of the multiexponential nature of the decaying signal.

4.2.5 Peak Width

To quantify the resolution of the main water peak in the T_2 distributions of figures 4.6 – 4.9, the peak widths were calculated. The peak width, analogous to the variance on a logarithmic scale, was calculated according to Whittall *et al* [16]. The widths was also calculated for the main water peak in the gray matter structures but were found to show minimal variation between the different pulse sequences, obvious figures 4.2 – 4.5. In white matter, where resolving the short T_2 myelin component was important in generating the NNLS solution, the width of the main peak in the distributions decreased as a function of the SES. The curves corresponding to where the SES was longest also showed a distinct myelin peak that couldn't be detected at shorter echo spacings. The change in width of the main water peak as a function of SES is illustrated in figure 4.11 for the posterior internal capsules and the minor forceps. Table 4.4 shows the mean width of the main peak in each white matter structure. As the peak width

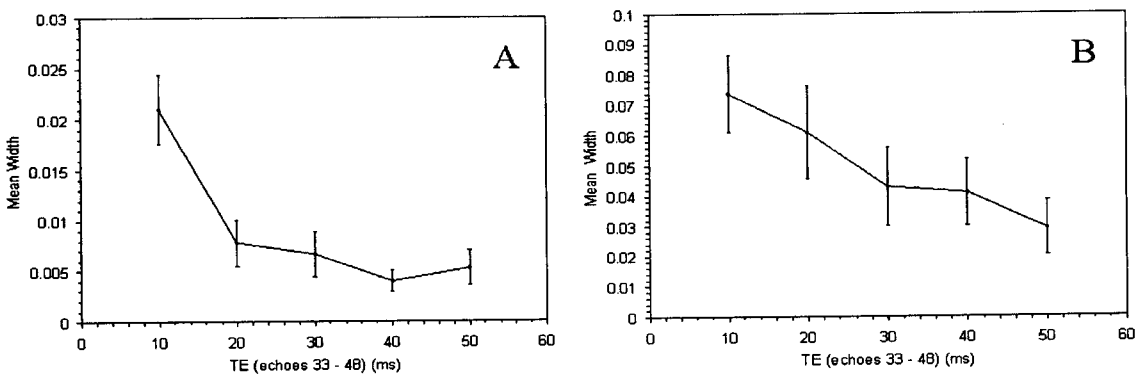

Figure 4.11: Mean width (♦) (standard errors) of the main water peak as a function of the secondary echo spacing in the A) minor Forceps and B) posterior internal capsules. Width decreased as the secondary echo spacing increased due to better sampling of the multiexponential decay curve at longer times.

decreased, the resolution increased, which allowed the T_2 characteristics of both the myelin and intra/extracellular water peaks to be better understood.

The decreased width (increased resolution) seen in the white matter main water peaks with longer secondary echo spacings was due to better sampling of the multiexponential decay curve. For an SES of 50 ms, the final echo was acquired at 1120 ms rather than at 480 ms when SES was only 10 ms. The longer acquisition time permitted the relaxation of the intra/extracellular component to be sampled more than twice as long. As a result, the NNLS fitting of the decay curve allowed more complete sampling and therefore the short T_2 component and the intermediate T_2 component were better resolved. A similar effect occurred for other increased SES times (ie. 20, 30, or 40 ms). The increased resolution of the main peak and the ability to better discern the location of the myelin peak without compromising important information is a clear benefit of employing longer echo spacings at the end of a pulse sequence. These longer secondary echo spacings lead to superior sampling of the decay curve, a necessity in accurately fitting the measured data.

Structure	TE (ms)	Mean Distribution Width	Distribution Width [16]
Genu of Corpus Callosum	10	0.0102 (0.0027)	0.014 (0.0045)
	20	0.0123 (0.0031)	
	30	0.0053 (0.0013)	
	40	0.0048 (0.0013)	
	50	0.0066 (0.0016)	
Minor Forceps	10	0.0210 (0.0034)	0.0091 (0.0035)
	30	0.0078 (0.0023)	
	30	0.0067 (0.0023)	
	40	0.0040 (0.0011)	
	50	0.0053 (0.0017)	
Posterior Internal Capsules	10	0.0738 (0.0127)	0.0709 (0.0069)
	30	0.0611 (0.0152)	
	30	0.0429 (0.0129)	
	40	0.0410 (0.0111)	
	50	0.0293 (0.0091)	
Splenium of Corpus Callosum	10	0.0222 (0.0047)	0.0466 (0.0075)
	30	0.0122 (0.0037)	
	30	0.0185 (0.0065)	
	40	0.0158 (0.0063)	
	50	0.0122 (0.0035)	

Table 4.4: The mean width (standard error) of the main water peak in 4 white matter structures for the 5 pulse sequences. The data are compared to previous results [16].

4.3 Conclusions

Normal volunteers were recruited to determine the effectiveness of alternative, variable echo pulse sequences on measuring T_2 relaxation properties in white and gray matter. From these *in-vivo* results several conclusions are drawn regarding the efficacy of using different echo spacings within a pulse sequence. By separating the pulse sequence into multiple sections, in this case two, greater information was extracted from a decay curve than if only a single, constant echo spacing was employed. Many current pulse sequences use a constant echo spacing throughout which forces the investigator to decide whether to use a short TE to maximize information about fast relaxing components or a longer TE to study components that undergo slower T_2 relaxation. While the longer SESs at the end of the pulse sequence did not dramatically improve the resolution of the main water peak in gray matter it was advantageous when examining various white matter regions. Our results demonstrated that an increased SES for the final 16 echoes of a 48-echo pulse sequence resulted in an increased resolution of both the short and long T_2 components in white matter.

Measurements of the geometric mean T_2 showed that each of the pulse sequences tested did well in reproducing the results of Whittall *et al.* [16]. A key difference between these two studies was that the Whittall study was limited to only 32 echoes with a constant echo spacing of 10 ms. Therefore, their study sampled the last echo at 320 ms. In our study the minimum time that the last echo was acquired was 480 ms but for a SES of 50 ms, this time was extended out to 1120 ms. Previous work has suggested that to accurately measure T_2, the decay curve should be sampled for at least 3 – 4 times longer than its longest relaxation time [47]. Clearly, extending the time at which the final echo was sampled aided in the analysis because it provided the NNLS algorithm with greater information about the behaviour of the intra/extracellular water compartment. Once the behaviour of this component was better understood, the myelin water compartment's contribution to the decay curve was more accurately determined. The reduced myelin water signal from gray matter resulted in little

improvement in resolution of the main water peak even when longer echo spacings were employed.

The resolution of the main water peak also improved substantially, as shown in figure 4.11 where the mean variance is plotted. As in the case of the geometric mean T_2, sampling the decay curve at longer times improved the accuracy of the NNLS solution. As the SES increased, a decrease in the width of the main peak was observed. This is a further benefit to the use of extended secondary echo spacings because the location of the intermediate T_2, intra/extracellular water component can be more accurately calculated.

The myelin water fractions were comparable for each of the white matter structures to the results of Whittall *et al.* However, the longer SES sequences yielded myelin peaks that were better resolved. It is hypothesized that the estimates of the MWF in the 4 white matter structures examined in this thesis are an improvement over the previous MWF measurements since sampling of the decay curve was increased at longer times.

Chapter 5 – Phantom Results

5.1 Introduction

It was shown in chapter 4 that when a 48-echo pulse sequence was altered to provide an extended secondary echo spacing (SES), it was possible to gain more information about the myelin and intra/extracellular water compartments of the brain. The study conducted in chapter 4 was performed on normal volunteers and it was expected that the T_2 distributions would yield only these two water compartments, when cerebrospinal fluid (CSF) was excluded. However, for patients afflicted with multiple sclerosis (MS), alterations in microscopic structure in lesions due to inflammation or edema might result in isolated water reservoirs. We anticipated that such pathological changes might cause an additional water compartment to appear in the T_2 distribution. The increase in mobility of the water in this lesion would lead to T_2 relaxation times that are greater than both myelin or intra/extracellular water but less than CSF.

$NiCl_2$ water phantoms were used to mimic the effect of additional water reservoirs on the T_2 decay curve of MS lesions in the absence of available volunteers afflicted with MS. As in chapter 4, 5 48-echo CPMG pulse sequences with two echo spacings were used for to image the phantoms. The primary echo spacing (PES), spacing of echoes 1 – 32, was 10 ms throughout, but the secondary echo spacing (SES), for echoes 33 – 48, was changed to 10, 20, 30, 40 and 50 ms over the 5 successive scans.

Eight $NiCl_2$ water phantoms exhibiting monoexponential T_2 relaxation were used in this study. The T_2 relaxation times of these phantoms ranged from 24 – 444 ms, with the phantoms being separated into 3 groups that represented the myelin, intra/extracellular and lesion water compartments. Eighteen different combinations of 3 water phantoms, one from each group, were created to generate triexponential decay curves. Furthermore, for each combination of 3 phantoms, the proportion that each phantom contributed to the triexponential decay was varied. Therefore a total of 54 unique T_2 distributions were created.

In this chapter, the results of the phantom study are presented. First, the decay curves from the individual phantoms and from the different combinations

are shown. The T_2 distributions generated from these decay curves are discussed followed by specific calculations that were made based upon them. These calculations include the geometric mean T_2 (GM T_2), the peak widths of the intra/extracellular and lesion water components and the myelin water fraction (MWF). Finally, the key results and conclusions will be discussed.

5.2 Results

5.2.1 T_2 distributions of Monoexponential Phantoms

Decay curves for each monoexponential phantom were calculated using regularized NNLS. For a SES of 50 ms, 2 decay curves are shown in figures 5.1A and 5.1B for T_2 times of 80 and 286 ms respectively. The curves in figure 5.1 are the best-fit solutions found by regularized NNLS. The 80 ms phantom decayed into the background noise all 48 echoes were sampled. To ensure that solving the data in the presence of background noise did not adversely affect the fit, the decay curves were truncated at 300 ms, well above the noise, and re-evaluated. The measured T_2 times for the truncated data set varied by less than 2 % from those calculated based on the NNLS solutions found using all 48 echoes. In figure 5.1B, the long relaxation time of the phantom meant that the last echo was acquired with a signal greater than the background noise and thus the fit to the data by NNLS was improved.

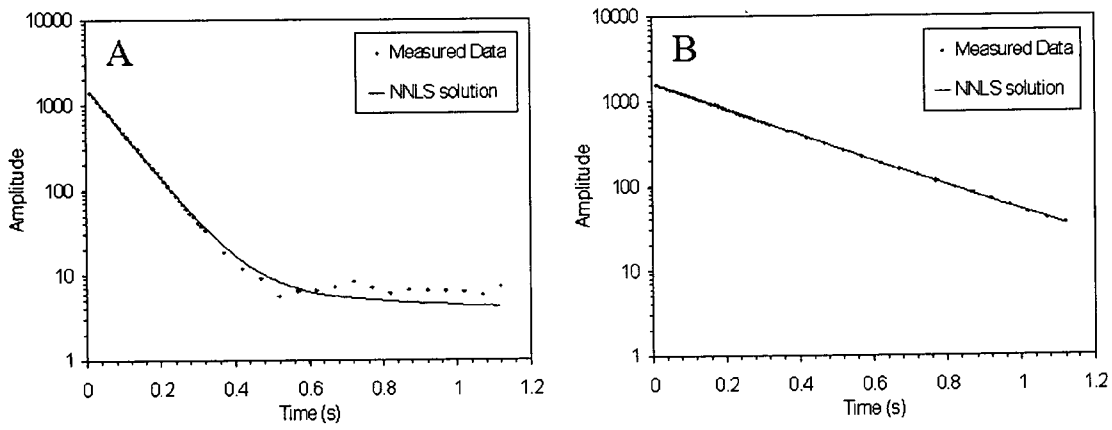

Figure 5.1: Measured decay curves (♦) and the NNLS solution of 2 $NiCl_2$ water phantoms with monoexponential relaxation. The T_2 times are A) 80 ms and B) 286 ms.

For confirmation of the T_2 for the phantoms, each was scanned using two additional 48-echo sequences with a constant TE. The first used a TE of 20 ms where the final echo was acquired at 960 ms and the second had TE set to 30 ms for that resulted in the decay curve being sampled to 1440 ms. The first of the 5 pulse sequences tested employed a PES and a SES of 10 ms which is equivalent to a constant TE of 10 ms. As a result, the T_2 for each phantom was measured by 3 constant TE sequences. The measured T_2 times from these 3 sequences and the average T_2 are shown in table 5.1. Only a small variation between the 3 sequences was observed. It was observed that the GM T_2 of the 80, 97 and 110 ms phantoms decreased as TE increased while the longest phantoms, 286 and 444 ms, steadily increased as TE increased. Currently, the mechanism that caused this effect is not well understood. The 24 and 29 ms phantoms were not scanned with constant echo spacings of 20 and 30 ms because their fast relaxing nature required closely spaced sampling of their decay curves.

For each of the 8 phantoms imaged, the NNLS algorithm was used to determine the T_2 distribution. Figures 5.2 show these 8 T_2 distributions of the monoexponential phantoms solved with regularized NNLS. The SNR per pixel of the measured data is also displayed and were comparable to those found for the gray matter structures discussed in chapter 4.

	Geometric Mean T_2 (ms)			
	TE = 10 ms	TE = 20 ms	TE = 30 ms	*Mean GM T_2*
Phantom # 1	24.4	-----	------	*24.4*
Phantom # 2	28.7	------	------	*28.7*
Phantom # 3	83.5	79.0	77.8	*80.1 (2.1)*
Phantom # 4	100.8	95.7	94.1	*96.8 (2.5)*
Phantom # 5	115.3	109.4	106.4	*110.3 (3.2)*
Phantom # 6	179.3	181.0	177.0	*179.1 (1.4)*
Phantom # 7	278.5	288.7	292.1	*286.4 (5.0)*
Phantom # 8	440.2	442.7	450.3	*444.4 (3.7)*

Table 5.1: Geometric mean T_2 of each of the 8 monoexponential phantoms prior to combining. Phantoms 1 and 2 were sufficiently short that their decay curves were sampled adequately by the single 48-echo sequence with TE = 10 ms.

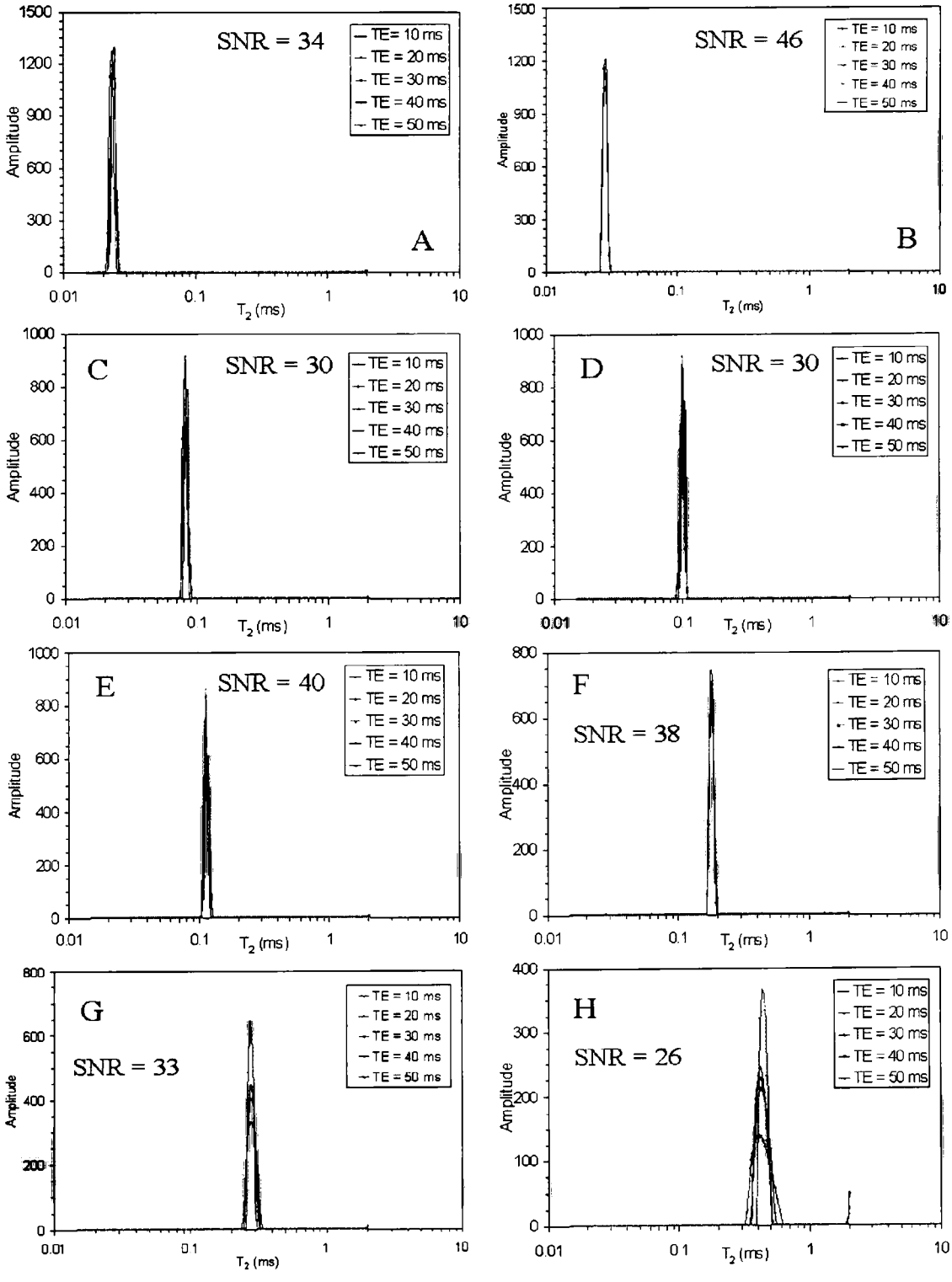

Figure 5.2: NNLS T_2 distributions for the 8 $NiCl_2$ phantoms for the 5 secondary echo spacings. A) 24 ms; B) 29 ms; C) 80 ms; D) 97 ms; E) 110 ms; F) 179 ms; G) 286 ms; H) 444 ms. The mean per pixel SNR for the 5 SESs are also shown.

5.2.2 T_2 Distributions of Multiexponential Combinations

To mimic the T_2 characteristics of cerebral tissue containing MS lesions associated with demyelination, the 8 monoexponential phantoms were combined in different combinations. They were separated into 3 groups representing the 3 principle water compartments (excluding CSF) detectable in MS patients. The first group contained the 24 and 29 ms phantoms, the 80, 97, and 110 ms phantoms in the second group, and the 179, 286 and 444 ms phantoms to simulate water associated with lesions. To combine these phantoms the normalized decay curves from a member of each group were added together. This produced a total of 18 triexponential combinations. The 18 combinations were split into 3 groups that represented the fraction of each phantom contained in the mixture. The 3 percentage contributions were 10:80:10, 15:70:15, and 15:75:10. A total of 54 triexponential decay curves were created and analyzed using NNLS.

For the fraction 10:80:10, the normalized decay curve from 2 of the 18 combinations and their calculated NNLS solutions are shown in figure 5.3. The error bars on the measured data are asymmetric due to the use of a logarithmic scale. As the SNR of the each monoexponential phantom varied, so did the SNR of the resultant combinations. On average, the per pixel SNR of the 54 combinations was approximately 100:1, only slightly greater than that of cerebral

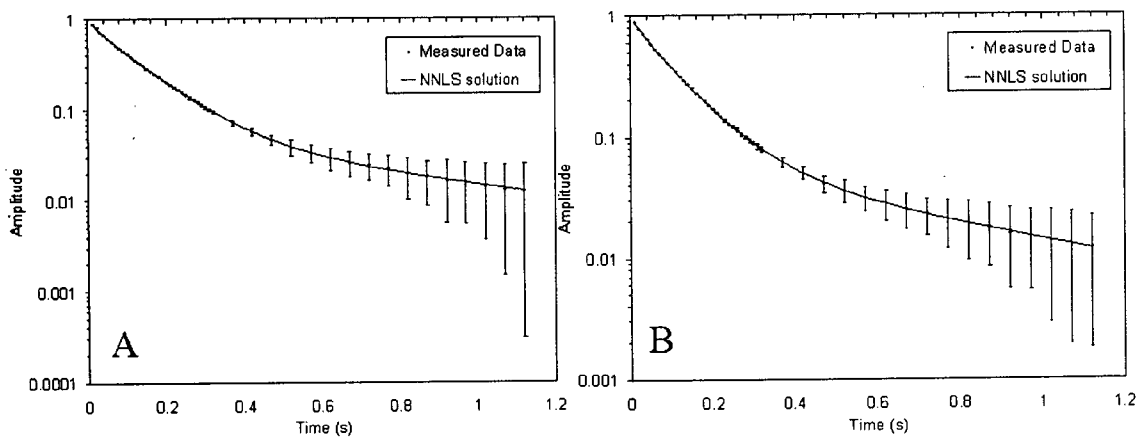

Figure 5.3: Decay curves (♦) for two different combinations of phantoms, in the ratio 10:80:10, collected with a secondary echo spacing of 50 ms. A) Mixture of 24, 110, and 444 ms T_2 relaxation times. B) Mixture of 28, 97, and 286 ms T_2 relaxation times.

white matter. This is important because the large majority of MS lesions are detected in the white matter of patients [48].

The T_2 distributions from the 54 decay curves were solved with the NNLS algorithm. The regularized NNLS solutions were preferred to the non-regularized method. The smoothed solution of regularized NNLS was preferred because the actual distribution in the brain is likely to not contain three distinct T_2 values, rather it would contain three distinct regions in the T_2 domain. The regularized and non-regularized NNLS solutions from two different combinations of monoexponential phantoms, in the proportions 10:80:10 and 15:70:15, are shown in figure 5.4. The regularized distributions of figures 5.5A and 5.5B are more applicable to a clinical situation where the 3 water compartments are shown as 3 narrow ranges of T_2 times. The non-regularized NNLS solutions are more sensitive to noise in the measured data that can lead to spurious spikes in the distribution, often times not reflecting the true T_2 characteristics.

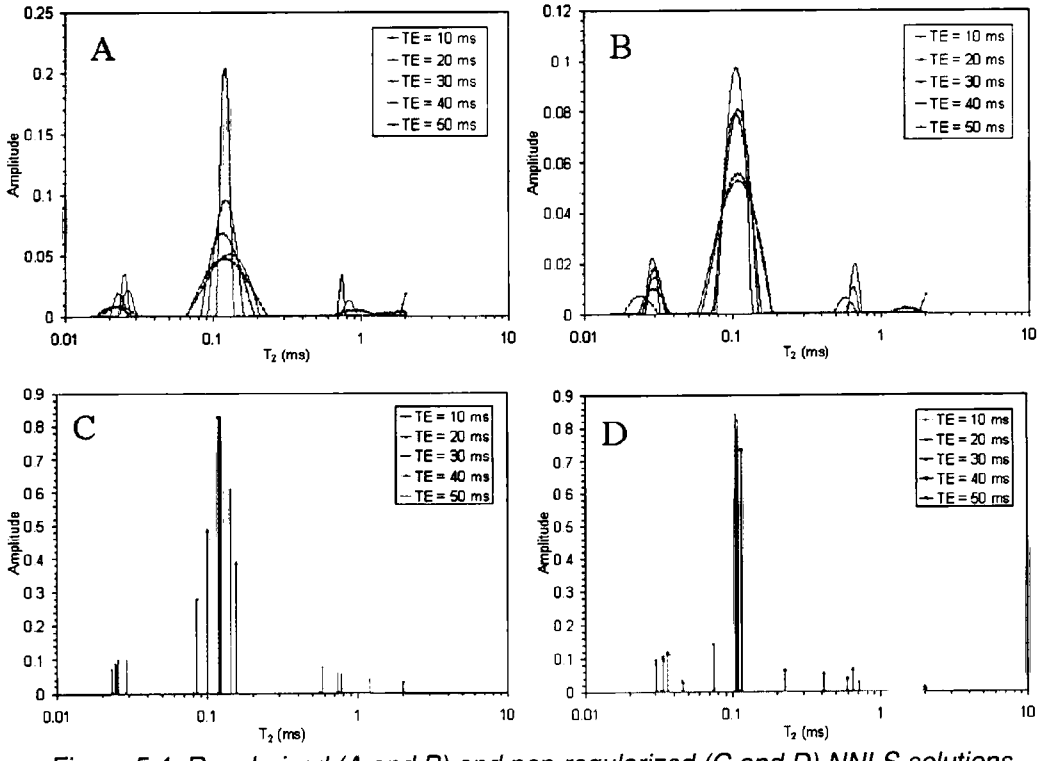

Figure 5.4: Regularized (A and B) and non-regularized (C and D) NNLS solutions of multiexponential phantoms. (A and C) 24, 110 and 444 ms phantom combination. (B and D) 28, 97 and 286 ms phantom combination.

For the duration of this chapter the results from 8 of the 54 T_2 distributions, 4 combinations in two different fractions, will be presented. These 8 distributions are representative of the effect of different proportions and combinations of phantoms on the ability of an extended SES to measure various parameters. Figures 5.5 - 5.6 illustrate the changes that occurred in the T_2 distributions, particularly in the intermediate and long T_2 components, when the combinations and fractions were altered.

In figures 5.5A and 5.5C, the distributions from the 24, 110 and 444 ms mixture, in the proportions 10:80:10 and 15:70:15 respectively, are shown. It is observed that as the fractional contribution of the short and long T_2 components were increased from 10% to 15% the location of the long T_2 peak shifted towards a lower T_2 value. As the SES increased, the resolution of this component also increased, demonstrated by the decreased width of the long T_2 peak. The increased resolution also was evident for both the intermediate T_2 (analogous to intra/extracellular water *in-vivo*) component and the short T_2 analogous to myelin water *in-vivo*) component. A similar decrease in T_2 and in the width of the intermediate and long T_2 peak is seen in figures 5.5B and 5.5D.

When the long T_2 component's contribution to the decay curve was changed from 10 % to 15 % there was a 50 % increase in the signal that originated from the late part of the distribution. This increase provided the NNLS algorithm with much more data from which it could determine T_2. The effect of increased signal is demonstrated in figures 5.5A and 5.5C and in figures 5.5B and 5.5D. As the proportion increases further, to the limit of a 100 % long T_2 component as in figure 5.2H, the estimation of T_2 improves.

As was shown *in-vivo*, the increased SES permitted sampling of the decay curve to longer times, which resulted in increased, although still overestimated, accuracy in the calculation of T_2 times for the long component. Better knowledge of this component lead to a more accurate determination of the short and intermediate T_2 components.

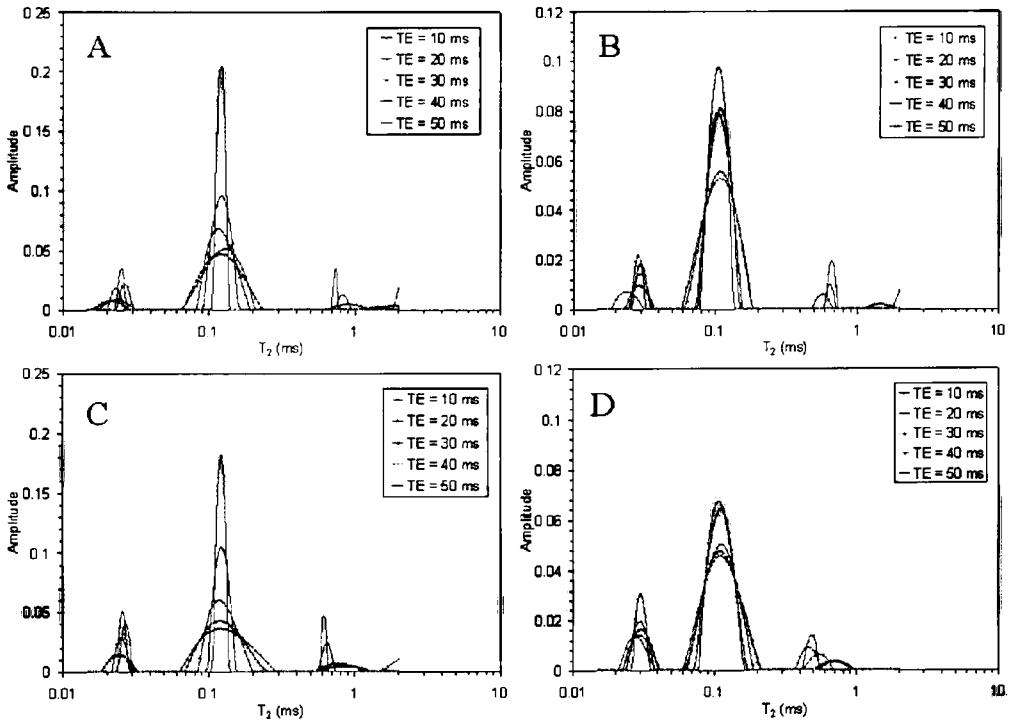

Figure 5.5: Regularized NNLS T_2 distributions for 2 mixtures of phantoms in 2 different fractions for the 5 pulse sequences. A) and C) are 24, 110 and 444 ms mixtures combined in 10:80:10 (A) and 15:70:15 (C). B) and D) are 29, 97 and 286 ms mixtures combined in 10:80:10 (A) and 15:70:15 (C).

Figures 5.6A and 5.6C show the results from another mixture that used the 444 ms phantom. As with figures 5.5A and 5.5C, the increased SES and the increased fraction of this component gave an estimate nearer the true T_2 for the long component than the sequences with a short SES. The result was consistent for all 18 distributions that used the 444 ms phantom for the long T_2 component. Furthermore, the increased accuracy of the long component through an extended SES increased the resolution of the myelin and main water peaks.

Figures 5.6B and 5.6D are representative of the 179 ms mixtures and illustrate an important finding of this study. A peak at 179 ms could not be resolved in any of the 18 mixtures for which this phantom was used regardless of the pulse sequences used. The GM T_2 of the main peak was however calculated to lie slightly higher than the true T_2. This result was caused by the closely spaced T_2 relaxation times of the two peaks that made it very difficult to discern

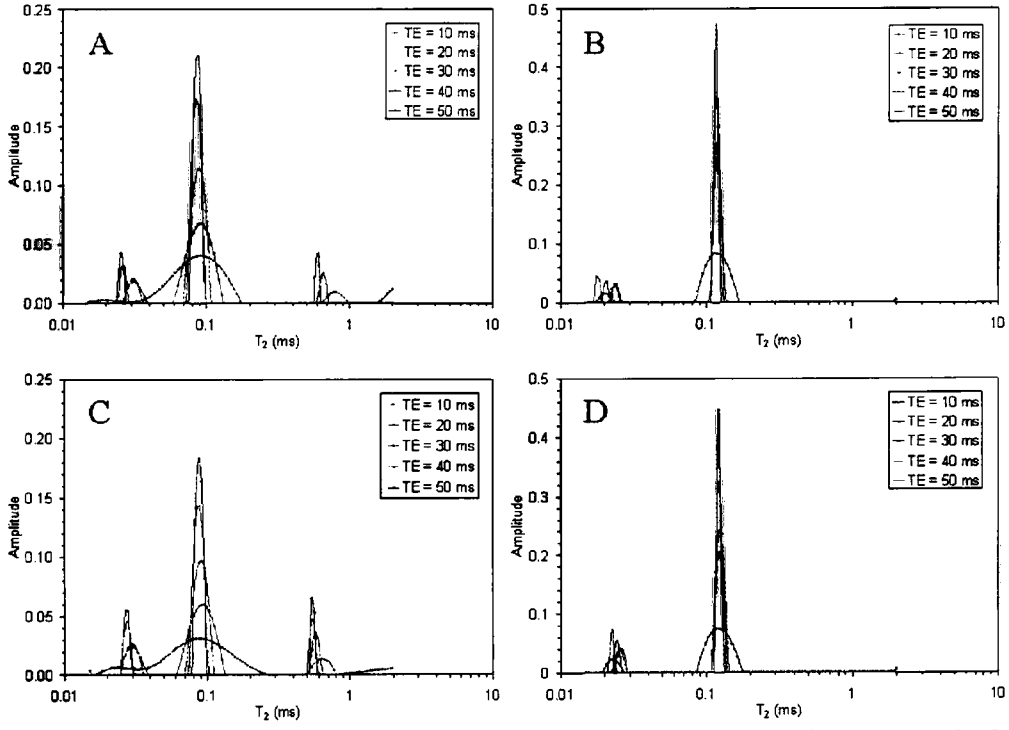

Figure 5.6: Regularized NNLS T_2 distributions for 2 mixtures of phantoms in 2 different fractions for the 5 pulse sequences. A) and C) are 24, 80 and 444 ms mixtures combined in 10:80:10 (A) and 15:70:15 (C). B) and D) are 24, 110 and 179 ms mixtures combined in 10:80:10 (A) and 15:70:15 (C).

two distinct time constants in this range. When the non-regularized NNLS routine was applied it also could not separate the two components. This is a significant result because it imposes a lower limit on the T_2 of a lesion that one should attempt to observe *in-vivo*. Specifically, adjacent components of a distribution should be separated by at least a factor of 2 or 3 if they are expected to be resolved from one another. If further study of MS lesions show that their true T_2 relaxation time is nearer to 200 ms then resolution of the main water and lesion water peaks would not be expected simply by extending the SES.

5.2.3 Geometric Mean T_2

The range over which the GM T_2 was calculated varied between the different mixtures because several distributions had large spacings (in T_2 space) between components while others did not. In all 54 mixtures, the upper bound on the myelin window was set to 50 ms, between two of the 120 T_2 partitions.

The lower bound on the main peak was also chosen as 50 ms, to prevent a component from being included in both windows. In 69 % of mixtures (37/54), the myelin and main peaks did not overlap this window and had values of zero on either side of the 50 ms limit. Fifteen of the remaining 17 combinations showed an overlap of this window for only one (typically SES of 10 ms or 20 ms) of the pulse sequences. The upper bound on the main peak fluctuated depending on which of the 3 phantoms was chosen for the long T_2 component, but was set at a constant 150 ms when the 179 ms phantom was chosen for the long T_2 component.

For the mixtures shown in figures 5.5 and 5.6, the GM T_2 of the intermediate and long T_2 components are given in table 5.2 for the 5 echo spacings studied. When the mixtures contained the 444 ms phantom, the long T_2 component was best estimated by the pulse sequences with the longest SES

Combination of T_2 (ms)	TE (ms)	Geometric Mean T_2 (ms)			
		Intermediate T_2 Component		Long T_2 Component	
		Fraction 1	**Fraction 2**	**Fraction 1**	**Fraction 2**
24, 110 and 440 ms	*10*	*120.6*	*124.8*	*913.9*	*781.0*
	20	*122.3*	*129.1*	*0*	*0*
	30	*120.9*	*124.7*	*1385.6*	*852.2*
	40	*120.8*	*123.1*	*829.2*	*648.4*
	50	*119.9*	*121.9*	*735.3*	*616.3*
28, 97 and 286 ms	10	107.0	110.8	572.7	458.5
	20	106.7	111.7	0	722.7
	30	107.6	112.8	0	687.9
	40	106.5	109.4	646.2	480.9
	50	103.8	110.3	664.7	542.6
24, 80 and 444 ms	*10*	*88.7*	*88.4*	*0*	*964.3*
	20	*89.2*	*91.6*	*795.11*	*635.0*
	30	*87.4*	*89.2*	*651.7*	*574.3*
	40	*85.9*	*87.9*	*595.6*	*545.4*
	50	*85.0*	*86.8*	*594.6*	*543.5*
24, 110 and 179 ms	10	117.1	118.9	158.4	161.4
	20	120.0	124.2	0	0
	30	119.2	123.8	0	0
	40	118.1	122.8	0	0
	50	117.4	122.2	0	0

Table 5.2: The GM T_2 of both the intermediate and long T_2 component from the T_2 distributions for 4 mixtures of phantoms in 2 different fractions. The two fractions used were 10:80:10 and 15:75:10. The GM T_2 of the long component was better approximated as TE increased.

(40 and 50 ms) for all fractions. As the proportion of the 444 ms phantom in the mixture increased, so did the accuracy of the GM T_2 estimate. Note that in all mixtures the GM T_2 calculated for the long component was higher than the true T_2. In the mixture that used the 286 ms phantom for the long component, two of the sequences (20 and 30 ms) did not detect a peak in the latter region of the distribution. A similar result was observed in the mixtures that used the 179 ms phantom. The only non-zero estimate for GM T_2 of the long component was made by the shortest SES (10 ms) however in this case part of the main peak extended across the 150 ms boundary into the third region of the distribution. In the 179 ms mixtures, the main peak was consistently overestimated due to poor resolution of the last two peaks in the distribution.

5.2.4 Myelin Water Fraction

To measure the ability of the different pulse sequences to detect the small, rapidly relaxing T_2 component due to myelin water, the myelin water fraction was calculated for each phantom combination. The myelin water fraction (MWF) was calculated as the proportion of signal that occurred within the window 0 – 50 ms, compared to the signal measured across the entire distribution. The measured MWFs for the 4 mixtures, for 2 fractions are shown in table 5.3. Fraction 1 and fraction 2 of table 5.3 represent the ratios 10:80:10 and 15:70:15 respectively so the calculated MWFs were expected to be 10 % and 15 % respectively.

Mixture Of T_2 (ms)	TE_2 (ms)	MWF (%)		Mixture Of T_2 (ms)	TE_2 (ms)	MWF (%)	
		Fraction 1	**Fraction 2**			**Fraction 1**	**Fraction 2**
24, 110 and 444 ms	*10*	*7.9*	*13.7*	*24, 80 and 444 ms*	*10*	*8.6*	*15.3*
	20	*7.5*	*12.5*		*20*	*10.9*	*17.1*
	30	*6.8*	*12.8*		*30*	*10.6*	*16.2*
	40	*9.0*	*14.7*		*40*	*9.8*	*16.0*
	50	*9.6*	*14.8*		*50*	*9.1*	*15.3*
29, 97 and 286 ms	10	8.2	14.2	24, 110 and 179 ms	10	7.2	12.6
	20	6.1	12.5		20	8.6	14.2
	30	7.5	13.9		30	8.5	14.3
	40	8.7	14.2		40	7.9	13.7
	50	8.8	13.6		50	8.2	13.8

Table 5.3: MWF from the short T_2 component in 4 mixtures of phantoms for 2 different fractions in the range 0 – 50 ms. Fractions 1 and 2 have % contributions of 10:80:10 and 15:70:15 respectively.

In the first mixture (24, 110, and 444 ms) of table 5.3, the accuracy with which the MWF was measured increased as the SES increased for both fractions shown. The same result was observed in the third fraction, 15:75:10. The accuracy for all 5 pulse sequences was better in the other 444 ms combination (24, 80 and 444 ms) phantoms where even the shortest SES allowed a MWF of 8.6 and 15.3 % to be calculated for fractions 1 and 2 respectively. For this combination of phantoms, the sequence with a 10 ms SES measured the MWF as accurately as a sequence where SES was 50 ms. For all the 444 ms combinations there was consistent increase in the MWF as longer SESs were employed.

When the MWF was calculated for second combination of phantoms (29, 97 and 286 ms) in table 5.3, the results were not as clear as for the 444 ms mixtures. From the table it is seen that there was not a SES that could consistently determine the MWF closest to its actual value. When the entire set of 286 ms phantoms were analyzed, the same result was seen. It did appear that the longer echo spacings were advantageous for determining the MWF, however it would be difficult to select one of the 40 and 50 ms spacings as best.

The fourth mixture (24, 110 and 179 ms) in table 5.3 measured MWFs that were comparable in accuracy to the 286 ms combinations even though the long T_2 peak could not be resolved from the main peak. Similar observations were made on the remaining 179 ms mixtures. This result implies that although the two latter peaks appeared to be due to a single relaxation event, the lack of resolution of these two peaks did not inhibit the detection of the signal emanating from the short myelin component.

As with the GM T_2 results above and for the peak width measurements to be presented in the next section, the accuracy of MWF calculations was dependent upon the separation of components in the T_2 distribution and on the SES when the components were spaced by several T_2 times. It would be beneficial for clinical use to more accurately measure the T_2 relaxation of MS lesions because the performance of different echo spacings depended upon the spacing of the T_2 components. The most accurate MWF measurements were

made when the T_2 times of each region were separated by at least a factor 3. For all 6 combinations that used the 444 ms phantom, and for the different fractions for these combinations, the measured MWF improved for a SES of 40 or 50 ms.

5.2.5 Peak Width

The widths of the peaks of both the intermediate and long components of the T_2 distributions were calculated to provide a measure of the resolution of the different secondary echo spacings. The 4 combinations of phantoms examined in sections 5.2.2 and 5.2.3 are presented in this section and were representative of the variations observed in the other phantom mixtures. The calculated peak widths for main water and lesion water regions for 2 of the 3 fractions used, 10:80:10 and 15:75:10, are shown below in table 5.4.

Combination of T_2 (ms)	TE (ms)	Peak Width (ms)			
		Intermediate T_2 Component		Long T_2 Component	
		Fraction 1	**Fraction 2**	**Fraction 1**	**Fraction 2**
24, 110, and 444 ms	*10*	*0.0337*	*0.0345*	*0.0207*	*0.0273*
	20	*0.0634*	*0.112*	*NP*	*NP*
	30	*0.0755*	*0.0752*	*0.0044*	*0.0352*
	40	*0.0152*	*0.0100*	*0.0031*	*0.0031*
	50	*0.0031*	*0.0031*	*0.0005*	*0.0007*
29, 97, and 286 ms	10	0.0246	0.0278	0.0057	0.0086
	20	0.0635	0.0716	0.0000	0.0163
	30	0.0547	0.0626	0.0000	0.0185
	40	0.0233	0.0297	0.0017	0.0037
	50	0.0142	0.0541	0.0021	0.0120
24, 80, and 444 ms	*10*	*0.0822*	*0.0887*	*0.0000*	*0.0011*
	20	*0.0301*	*0.0285*	*0.0089*	*0.0114*
	30	*0.0095*	*0.0102*	*0.0015*	*0.0022*
	40	*0.0028*	*0.0026*	*0.0004*	*0.0005*
	50	*0.0042*	*0.0046*	*0.0004*	*0.0013*
24, 110, and 179 ms	10	0.0204	0.0202	0.0004	0.0012
	20	0.0025	0.0032	NP	NP
	30	0.0019	0.0022	NP	NP
	40	0.0012	0.0012	NP	NP
	50	0.0008	0.0008	NP	NP

Table 5.4: Width of the intermediate and long T_2 components in 4 combinations of phantoms for 2 fractions tested. Fractions 1 and 2 have % contributions of 10:80:10 and 15:70:15 respectively. NP corresponds to distributions in which no peak was observed for a specific component.

For the first mixture (24, 110 and 444 ms) in table 5.4, the widths of both peaks decreased as the SES increased from 10 to 50 ms. Although the GM T_2 of the long T_2 component in this mixture was better approximated when its fraction was increased to 15 %, the peak width showed no decrease as the fraction was raised. For the other 444 ms mixture (24, 80 and 444 ms), the SESs of 40 and 50 ms resulted in large improvements in the peak width but again the width did not depend upon the fraction. For the remaining 444 ms mixtures, a similar result was observed where the resolution increased as SES increased but showed only minor variations in width as the fraction of its contribution to the mixture increased. For all the 444 ms mixtures, as the resolution of the latter peak improved so did the resolution of the main water peak. This observation corresponds to better separation of the intermediate and long T_2 components from the measured data due to longer sampling of the decay curve.

For the second mixture (29, 97 and 286 ms) in table 5.4 the width improved at longer values of the SES, however the increased fraction of the long component did not appear to contribute to the decreased width. Also, the width of the main peak showed large variations between different SES. Analysis of the set of 286 ms combinations could not identify a SES that consistently yielded a low peak width for the main water compartment.

In the set of 179 ms mixtures, and the last mixture (24, 110 and 179 ms) of table 5.4, the long T_2 component could not be resolved from the main water peak. Therefore in these combinations the widths were measured to be zero in within the third region of the T_2 distribution (T_2 > 150 ms) . The width of the main peak in these phantoms was very low compared with the other mixtures. The decreased width was a due to the inability to resolve the two components due to their closely spaced T_2 relaxation times. Therefore the portion of the distribution between 80 and 180 ms was solved for using a single exponential term.

5.3 Conclusions

A 48-echo pulse sequence employing 5 different secondary echo spacings, from 10 – 50 ms, was used to image a series of $NiCl_2$ water phantoms

whose T_2 relaxation times ranged from 24 – 444 ms. The phantoms were scanned individually to generate a series of monoexponential decay curves which were then normalized and combined into a series of mixtures. These mixtures were created such that their relaxation characteristics simulated those expected from cerebral tissue containing multiple sclerosis lesions.

We found that the performance of the pulse sequences was dependent upon more than one factor. These included the proportion of each component in the T_2 distribution and the separation of the T_2 components in the T_2 distribution. For the mixtures that contained a long T_2 component of 444 ms, the measurement of the GM T_2, the peak width and the MWF all improved as the SES increased. If it is assumed that the true T_2 of MS lesions are on the order 400 – 500 ms, there would be a definite clinical benefit in using an extended SES. This study showed that such a pulse sequence improves the resolution of the both intermediate and long T_2 peaks through a decrease in the peak widths. At the same time the longer sequences better estimate the proportion of the signal contributed by the short T_2 component. Extended decay curve sampling provides more information about the decay characteristics, leading to a better fit to the data.

Conversely, in the set of 6 mixtures where the longest T_2 was 179 ms, the main peak and lesion water peak were too closely spaced to permit separation of their components from the decay curve. As a result the T_2 distribution yielded a very narrow intermediate peak whose T_2 was shifted to a slightly higher value than the true intermediate T_2. In these mixtures, the lack of resolution of the two longest water compartments did not adversely affect the measurement of the signal emanating from the fast relaxing myelin water component.

In the remaining 6 mixtures, where the longest T_2 was 286 ms, increasing the SES did not greatly improve the measured MWF. The width of the main peak also did not show a substantial decrease as the SES increased. However, the GM T_2 did exhibit a small improvement in estimating the slow relaxing component when shorter SESs were used.

As a clinical tool, the longer pulse sequences (40 and 50 ms) are of benefit if the area under interest has multiple relaxing components and if the relaxation times of these components differ from one another by a factor of three or more. In this situation, the decay curves are sampled to longer times and the different decay curves contributing to the measured signal can be best resolved. Also, imaging regions where the longer T_2 components are a large proportion of the measured signal will increase the accuracy of the T_2 estimates, because the longer echo spacings permit better sampling of the decay characteristics of the curve. An increased proportion simply causes the long component to contribute more to the decay curve. This effect was particularly noticeable in the 6 mixtures where the 444 ms phantom was used for the long T_2 component.

Chapter 6 – Conclusions

6.1 In-vivo Study

Ten normal volunteers were imaged using a 48-echo pulse sequence with 5 different secondary echo spacings, 10, 20, 30, 40, and 50 ms. The goal of this *in-vivo* study was to determine whether an extended echo spacing could be employed without compromising valuable information about the short T_2 component is associated with water compartmentalized within myelin. By separating a pulse sequence into 2 sections, greater information was extracted from the decay curves than when only a single constant echo spacing was utilized. The extended secondary echo spacing showed that in white matter, the resolution of the main water peak associated with intra/extracellular water was improved and that multiple water reservoirs were present. The presence of only a single main water peak in gray matter indicated that the distribution of water is homogeneous within gray matter structures and the water molecules are not restricted to specific compartments.

When the geometric mean T_2 was measured, each of the 5 pulse sequences were able to achieve GM T_2 values that were consistent, but lower, than those found previously for the main water peak [16]. In previous work, a 32-echo CPMG sequence with a constant TE of 10 ms was used to find the geometric mean T_2, peak widths and myelin water fractions. Our study used a 48-echo sequence with an extended secondary echo spacing that could sample the decay curves at much longer times, up to 1120 ms, and therefore more information was extracted about the decay curve. We demonstrated that the increased sampling of the decay curves was beneficial because it allowed both the myelin and main water contributions to be more accurately determined. In gray matter, the low signal from myelin water resulted in little improvement in resolution of the main water peak even when longer echo spacings were employed.

When the calculated myelin water fractions were compared to those measured previously, we found good agreement in each of the white matter

structures [16]. As with the measurements of GM T_2, we believe that these measurements are more accurate than those of Whittall *et al.* due to better sampling of the decay curve. The longer SES sequences provided myelin peaks that were better resolved, however at this time it is not possible to comment on the GM T_2 of the myelin peaks. The very short T_2 of myelin water coupled with the relatively long primary echo spacing of 10 ms causes difficulty in estimating the T_2 of this component.

We have demonstrated that in white matter there was a benefit to the use of longer echo spacings at the end of the pulse sequence. Longer secondary echo spacings yield greater information about the nature of the decay curve and thus the T_2 distribution of the region being sampled. Longer sequences also can be performed without sacrificing any of the valuable information contained at short times because the early part of the pulse sequence can still be set to employ a short echo spacing.

6.2 Phantom Study

As in the human volunteer experiments, five 48-echo pulse sequences were tested on a series of $NiCl_2$ water phantoms using the same secondary echo spacings. Monoexponential decay curves were normalized and combined into a series of triexponential mixtures. The mixtures were created such that their relaxation characteristics simulated those expected from cerebral tissue containing multiple sclerosis lesions.

The ability of the different pulse sequences to accurately determine the T_2 of the components in the mixtures was dependent upon multiple factors. In the mixtures that contained a long T_2 component of 444 ms, the measurement of the GM T_2, the peak width and the MWF all improved as the SES increased. If it is assumed that the true T_2 of MS lesions are on the order 400 – 500 ms, then these results would indicate that there is a definite clinical benefit to using an extended SES. We showed that extended pulse sequences improved the resolution of the both intermediate and long T_2 peaks through a decrease in the peak widths. The longer sequences also estimated the proportion of the signal

originating from the short T_2 component more accurately. When the long component was separated by the intermediate component by at least a factor of 3 in the T_2 times, the extended decay curve sampling provided more information about the decay characteristics, leading to a better fit to the data.

Conversely, in the set of 6 mixtures where the longest T_2 was 179 ms, the main peak and lesion water peak were too closely spaced to permit separation of their components from the decay curve. This led to an interesting finding in that the T_2 distribution yielded a very narrow intermediate peak whose T_2 was shifted to a slightly higher value than the true intermediate T_2. The clinical implication of the results for the 179 ms phantoms was that the lesion water compartment must be separated by a larger amount in the T_2 domain if it is expected to be resolved from the strong main water peak. However, the poor resolution of the main and lesion water compartments did not adversely affect the measurement of the fast relaxing myelin component as the myelin water fractions were similar to those calculated with the 444 ms phantoms.

For the other 6 mixtures, where the longest T_2 was 286 ms, an increased SES did not greatly improve the measured MWF nor did it improve the resolution of the main water peak. The GM T_2 did exhibit a small improvement in estimating the slow relaxing component when shorter secondary echo spacings were used.

The phantom study and the *in-vivo* study demonstrated that an extended secondary echo spacing is a clinically useful tool when examining regions that are characterized by multiple relaxing components. Furthermore, the longer pulse sequences tested, particularly 40 and 50 ms, increased the measurements of the myelin water fraction, the peak width and the geometric mean T_2 when the different T_2 components differed by a factor of three or more. When this condition was satisfied, the sampled decay curves were separable into their different components. It was also shown that whenever possible imaging regions where the longer T_2 components are a greater proportion of the measured signal increases the accuracy of the T_2 estimates. The increased proportion of the long component causes it to contribute more to the decay curve. This effect was

particularly noticeable in the 6 mixtures where the 444 ms phantom was used for the long T_2 component.

6.3 Future Work

To better understand the efficacy of longer secondary echo spacings several more experiments need to be performed. The most important and clinically relevant of these would be to employ the same pulse sequences that were evaluated as part of this thesis on actual multiple sclerosis patients. A small study on MS patients would allow a direct comparison to be made with the findings of this study and also would provide much needed data regarding the T_2 relaxation time of the lesion water compartment. Much of the current knowledge of T_2 in lesions is based upon the hypothesis that lesion formation results in the creation of additional water reservoirs. These reservoirs are expected to contain water in a state of higher mobility than when it is confined to myelin or the intra/extracellular regions. It is important to know to greater accuracy the true range of T_2 for the lesion water compartment. By doing so, it would be possible to further optimize pulse sequences to target the T_2 of the lesion.

A second experiment that needs to be examined in the near future would be determine whether or not the myelin peak that was shown in chapter 4 for the longer secondary echo spacings is real. If it is, then longer secondary echo spacings would be even more advantageous because they were shown here to be able to extract the fast relaxing component from the decay curve better. Currently, there is great difficulty in determining the T_2 of the myelin component accurately because of practical limitations of the scanner. The echo spacing of clinical scanners often can not be set below 6 or 7 ms however the relaxation time of the myelin component is on the order of 20 to 30 ms and could be as low as 15 to 20 ms. The component relaxes very fast compared to the echo spacing used which means that only a handful of points on the decay curve can be sampled before the signal decays into the background noise or is overcome by the slower relaxing main water component.

Bibliography

1. J. Beatty. *The Human Brain – Essentials of Neuroscience.* Sage Publications, London. 2001.

2. A. J. Vander, J. H. Sherman, and D. S. Luciano. *Human Physiology: The Mechanisms of Body Function.* McGraw-Hill Publishing, New York, 6th Edition. 1994.

3. B. Alberts, D. Bray, J. Lewis, M. Raff, K. Roberts, and J. D. Watson. *Molecular Biology of the Cell.* Garland Publishing, New York, 3rd Edition. 1994.

4. J. H. Noseworthy, L. Lucchinetti and M. Rodriguez. Multiple sclerosis. *N. Engl. J. Med.* **343**:938 – 952. Sep 28, 2000.

5. R. Hohlfeld. Biotechnological agents for the immunotherapy of multiple sclerosis: principles, problems and perspectives. *Brain.* **120**:865 – 916. 1997.

6. A. D. Sadovnick, H. Armstrong and G. P. Rice. A population-based study of multiple sclerosis in twins: update. *Ann. Neurol.* **33**:281 – 285. 1993.

7. A. D. Sadovnick, P. A. Baird and R. H. Ward. Multiple sclerosis: updated risks for relatives. *Am. J. Med. Genet.* **29**:533 – 541. 1988.

8. D. Katz, J. K. Taubenberger, B. Cannella, D. E. McFarlin, C. S. Raine and H. F. McFarland. Correlation between magnetic resonance imaging findings and lesion development in chronic, active multiple sclerosis. *Ann. Neurol.* **34**:661 – 669. 1993.

9. W. I. McDonald. Rachelle Fishman-Matthew Moore lecture. The pathological and clinical dynamics of multiple sclerosis. *J. Neuropathol. Exp. Neurol.* **53**:338 – 343. 1994.

10. C. Raine. The neuropatholdy of multiple sclerosis. In: C. S. Raine, W. Tourtellotte, eds. *Multiple Sclerosis: clinical and pathogenetic basis.* Chapman and Hall, London. 1997.

11. H. F. McFarland. The lesion in multiple sclerosis: clinical, pathological, and magnetic resonance imaging considerations. *J. Neurol. Neurosurg. Psychiatry.* **64**:S26 – S30. May 1998.

12. N. de Stefano, S. Narayanan, R. Arnaoutelis, M. C. Tartaglia, J. P. Antel, P. M. Matthews and D. L. Arnold. Evidence of axonal damage in the early stages of multiple sclerosis and its relevance to disability. *Arch. Neurol.* **58**:65 – 70. 2001.

13. M. A. Lee, A. M. Blamire, S. Pendlebury, K. Ho, K. R. Mills, P. Styles, J. Palace and P. M. Matthews. Axonal injury or loss in the internal capsule and motor impairment in multiple sclerosis. *Arch. Neurol.* **57**:65 – 70. 2000.

14. J. Hoppner, E. Kunesch, J. Buchmann, A. Hess, A. Gropmann, and R. Benecke. Demyelination and axonal degeneration in corpus callosum assessed by analysis of transcallosally mediated inhibition in multiple sclerosis. *Clin. Neurophys.* **110**:748 – 756. 1999.

15. A. L. MacKay, K. P. Whittall, J. Adler, D. K. B. Li, D. Paty and D. Graeb. *In-vivo* visualization of myelin water in brain by magnetic resonance. *Magn. Reson. Med.* **31**:673 – 677. 1994.

16. K. P. Whittall, A. L. MacKay, D. A. Graeb, R. A. Nugent, D. K. B. Li, and D. Paty. *In-vivo* measurement of T_2 distributions and water contents in normal human brain. *Magn. Reson. Med.* **37**:34 – 43. 1997.

17. R. S. Menon and P. S. Allen. Application of continuous relaxation time distribtuions to the fitting of data from model systems and excised tissue. *Magn. Reson. Med.* **20**:214 – 227. 1991.

18. W. A. Stewart, A. L. MacKay, K. P. Whittall, G. R. W. Moore and D. W. Paty. Spin-spin relaxation in experimental allergic encephalomyelitis: analysis of CPMG data using a non-linear least-squares method and linear inverse theory. *Magn. Reson. Med.* **29**:767 – 775. 1993.

19. H. W. Fischer, P.A. Rinck, Y. V. Haverbeke and R. N. Muller. Nuclear relaxation of human brain gray and white matter: analysis of field dependence and implications for MRI. *Magn. Reson. Med.* **16**:317 – 334. 1990.

20. R. M. Henkelman, G. J. Stanisz, J. K. Kim and M. J. Bronskill. Anisotropy of NMR properties of tissues. *Magn. Reson. Med.* **32**:592 – 601. 1994.

21. R. Harrison, M. J. Bronskill and R. M. Henkelman. Magnetization transfer and T_2 relaxation components. *Magn. Reson. Med.* **33**:490 – 496. 1995.

22. V. Vasilescu, E. Katona, V. Simplaceanu and D. Demco. Water compartments in myelinated nerve III Pulsed NMR results. *Experientia.* **34**:1443 – 1444. 1978.

23. M. D. Does and R. E. Snyder. T_2 relaxation of peripheral nerve measured *in-vivo. Magn. Reson. Imaging.* **13**:575 – 580. 1995.

24. K. P. Whittall and A. L. MacKay. Quantitative interpretation of NMR relaxation data. *J. Magn. Reson.* **84**:134 – 152. 1989.
25. H. B. Larsson, J. Frederiksen, L. Kjaer, O. Henriksen and J. Olesen. In vivo determination of T1 and T2 in the brain of patients with severe but stable multiple sclerosis. *Magn. Reson. Med.* **7(1)**:43 – 55. 1988.

26. H. B. Larsson, J. Frederiksen, J. Petersen, A. Nordenbo, I. Zeeberg, O. Henriksen and J. Olesen. Assessment of demyelination, edema, and gliosis by in vivo determination of T1 and T2 in the brain of patients with acute attack of multiple sclerosis. *Magn. Reson. Med.* **11(3)**:337 – 348. 1989.

27. J. P. Armspach, D. Gounot, L. Rumbach and J. Chambron. *In-vivo* determination of multiexponential T_2 relaxation in the brain of patients with multiple sclerosis. *Magn. Reson. Imaging.* **9**:107 – 113. 1991.

28. L. Rumbach, J. P. Armspach, D. Gounot, I. J. Namer, J. Chambron, J. M. Warter and M. Collard. Nuclear magnetic resonance T_2 relaxation times in multiple sclerosis. *J. Neurol. Sci.* **104**:176 – 181. 1991.

29. C. N. Chen and D. I. Hoult. *Biomedical Magnetic Resonance Technology.* Adam Hilger, New York. 1990.

30. R. A. Serway. *Physics For Scientists and Engineers.* Saunders College Publishing, Toronto, 3rd Edition. 1992.

31. I. I. Rabi, J. R. Zacharias, S. Millman, and P. Kusch. A new method of measuring nuclear magnetic moments. *Phys. Rev.* **53**:318 . 1938.

32. I. I. Rabi, S. Millman, P. Kusch, and J. R. Zacharias. The molecular beam resonance method for measuring nuclear magnetic moments. *Phys. Rev.* **55**:526 – 535. 1939.

33. F. Bloch, W. W. Hansend, an M. Packard. Nuclear Induction. *Phys. Rev.* **69**:127. 1946.

34. F. Bloch. Nuclear Induction. *Phys. Rev.* **70**:460 - 474. 1946.

35. E. M. Purcell, H. C. Torrey, and R. V. Pound. Resonance absorption by nuclear magnetic moments in a solid. *Phys. Rev.* **69**:37 - 38. 1946.

36. K. S. Krane. *Introductory Nuclear Physics.* John Wiley & Sons Publishing, New York. 1987.

37. C. Kittel. *Introduction to Solid State Physics.* John Wiley & Sons Publishing, New York, 7th Edition. 1996.

38. R. H. Hashemi and W. G. Bradley. *MRI: The Basics*. Williams and Wilkins, Philadelphia. 1997.

39. J. C. Mazziotta and S. Gilman. *Clinical Brain Imaging: Principles and Applications*. F. A. Davis Co., Philadelphia. 1992.

40. C. P. Slichter. *Principles of Magnetic Resonance*. Springer-Verlag, New York, 3rd Edition. 1990.

41. E. L. Hahn. Spin echoes. *Phys. Rev.*, **80**:580 – 584. 1950.

42. H. Y. Carr and E. M. Purcell. Effects of diffusion on free precession in nuclear magnetic resonance experiments. *Phys. Rev.*, **94**:630 – 638. 1954.

43. S. Meiboom and D. Gill. Modified spin echo method for measuring relaxation times. *Rev. Sci. Instr.*, **29**:688-691. 1958.

44. M. D. Mitchell, H. L. Kundel, L. Axel and P. M. Joseph. Agarose as tissue equivalent phantom material for NMR imaging. *Magn. Reson. Imaging.*, **4**:263 – 266. 1986.

45. J. O. Christoffersson, L. E. Olsson and S. Sjoberg. Nickel-doped agarose gel phantoms in MR imaging. *ActaRad.*, **32**:426 – 431. 1991.

46. K. A. Kraft, P. P. Fatouros, G. D. Clarke and P. R. S. Kishore. An MRI phantom material for quantitative relaxometry. *Magn. Reson. Med.*, **5**:555 – 562. 1987.

47. H. B. W. Larsson, G. J. Barker and A. L. MacKay. Nuclear magnetic resonance relaxation in multiple sclerosis. *J. Neurol. Neurosurg. Psychiatry.* **64**:S70 – S76. 1998.

48. R. Bakshi, J. Dmochowski, Z. A. Shaikh and L. Jacobs. Gray matter T2 hypointensity is related to plaques and atrophy in the brains of multiple sclerosis patients. *J. Neurol. Sci.* **185**:19 – 26. 2001.

49. Q.-S. Xiang. Introduction to MRI. Class notes: UBC-PHYS404, 2000.